Predicting Strong Motions for Seismic Hazard Assessments in Seattle, Washington

Andrew A. Delorey

A dissertation

submitted in partial fulfillment of the

requirements for the degree of

Doctor of Philosophy

2010

Program Authorized to Offer Degree:

Earth and Spaces Sciences

University of Washington
Graduate School

This is to certify that I have examined this copy of a doctoral dissertation by

Andrew A. Delorey

and have found that it is complete and satisfactory in all respects,
and that any and all revisions required by the final
examining committee have been made.

Chair of the Supervisory Committee:

____
John E. Vidale

Reading Committee:

____
John E. Vidale

____
Paul Bodin

____
Kenneth C. Creager

Date:____________________________________

In presenting this dissertation in partial fulfillment of the requirements for the doctoral degree at the University of Washington, I agree that the Library shall make its copies freely available for inspection. I further agree that extensive copying of the dissertation is allowable only for scholarly purposes, consistent with “fair use” as prescribed in the U.S. Copyright Law. Requests for copying or reproduction of this dissertation may be referred to ProQuest Information and Learning, 300 North Zeeb Road, Ann Arbor, MI 48106-1346, 1-800-521-0600, to whom the author has granted “the right to reproduce and sell (a) copies of the manuscript in microform and/or (b) printed copies of the manuscript made from microform.”

Signature ________________________

Date ____________________________

TABLE OF CONTENTS

List of Figures

Introduction

Forecasting earthquake recurrence rates then predicting strong motions generated by forecasted earthquakes and their effect on engineered structures is the essence of seismic hazard analysis. We use observations of past events to the extent that they exist to guide forecasts for recurrence rates and predictions of ground motions, however instrumental observations are unavailable for the majority of plausible damaging earthquake scenarios even in the best-instrumented regions and will likely remain that way for some time. Widespread instrumentation has only been around for decades or less depending on the location and is still non-existent in many places around the world. Because earthquake recurrence rates are often hundreds to thousands of years, well-recorded large events are scarce even in locations that are well instrumented. Due to the scarcity of instrumental observations of damaging earthquakes we are forced to base forecasts and predictions on indirect observations like trenching faults *e.g.* [*Nelson et al.*, 2003], or searching the sedimentary record for indications of landslides, uplift, subsidence, tsunami deposits or other earthquake markers *e.g.* [*Atwater*, 1992; *Witter et al.*, 2003].

Since recordings of large earthquakes are scarce, we must attempt to model the resulting ground motions using geophysical models. In order to model earthquake induced ground motions at the frequencies in which engineered structures are most vulnerable (0.2-1 Hz), at the scale of an urban neighborhood, we must know the shear wave velocity structure on the same scale, including the location of large velocity discontinuities that can occur across faults or other geologic boundaries. In addition, we need to know the velocities, thicknesses, and non-linear behavior of shallow, unconsolidated sediments [*Frankel et al.*, 2007]. Even in regions that are well studied, this level of detail is elusive.

I will present an approach to measuring shear wave velocities in the upper crust on the scale of a typical urban area that requires neither earthquakes nor active sources, with the potential to produce sub-kilometer resolution. In addition I will present some observations of how engineered structures respond to both ambient and earthquake generated shaking. Engineering analysis of structural response is often highly idealized so measurement of structures in their real environment is essential to understanding their vulnerabilities. Lastly, I will discuss some potential problems with broadband instruments recording moderate levels of shaking at local and regional distances.

The current seismic hazard map for Seattle is constructed using a Probabilistic Seismic Hazard Analysis (PSHA) [*Frankel et al.*, 2007]. There are two main inputs to a PSHA: a set of probabilities for all of the realistic damaging earthquake scenarios for the study area, and a prediction of the level of shaking that will be generated from each of the damaging earthquake scenarios. Both of these inputs involve making decisions with incomplete information since we do not precisely know earthquake recurrence rates, nor can we easily predict the resulting ground motions. In this study, I address improving ground motion predictions.

Earthquake recurrence rates are known reasonably well for some scenarios, and very poorly for others. Recurrence rate forecasts are usually based on the premise that activity observed in the past will continue into the future in roughly the same manner, but our knowledge of past earthquake activity usually only goes back a few thousand years, a short period of time in geologic history. Some earthquake cycles are short enough to have been observed multiple times like on the Parkfield section of the San Andreas Fault [*Murray and Langbein*, 2004]. Sometimes predictions are made by observing clustering and propagating sequences like on the Anatolia Fault [*Pondard et al.*, 2007]. Geodetically measured crustal deformation rates are sometimes used to estimate earthquake recurrence intervals as well [*Mazzotti et al.*, 2002] by estimating the long-term moment release then distributing the moment release across many events by using a magnitude relationship like the Gutenberg–Richter law. A challenging aspect of probability estimation is that we often never get a chance to test the predictions.

Predicting the level of shaking for various realistic earthquake scenarios is also difficult but we sometimes can test predictions by using a few representative earthquakes. In Seattle, there are recordings for the 2001 Nisqually 6.8 earthquake [*Frankel et al.*, 2002], but no other event of that size or larger has been as widely recorded in the area. So, we must rely on this event and a collection of smaller events to validate models and predictions. Despite these limitations, the current hazard maps and the additional predictions made in this study still offer a sound basis for hazard planning. Since a PSHA is based on statistics and predictions from many events, unless a substantial majority of the individual predictions are biased in the same direction, the overall outcome will be a reasonable representation of the risk. It is far worse to do nothing at all.

Two events that occurred in 2010 offer an excellent comparison of how two different societies suffered from a large earthquake: the 2010 Haiti 7.0 event and the 2010 Chile 8.8 event. According to news reports, the death toll in Haiti was over 200000 and only ~500 in Chile. The primary cause for the higher death toll in Haiti was poverty, resulting in inadequate preparation and response. However, it also shows that with the right information and resources we can prepare for earthquake hazards and significantly reduce the death toll and loss of infrastructure.

Seattle Basin Tomography

Seattle, Washington, one of the biggest cities in the United States that is threatened by earthquakes, sits atop a deep sedimentary basin. Nearby, Everett and Tacoma, Washington have a similar setting (Figure A1). These basin structures are the result of the evolution of the Puget Lowland fore arc basin, which combines strike-slip and thrust-fault earthquakes to accommodate right-lateral strike-slip and N-S shortening [*Johnson et al.*, 1996; *Pratt et al.*, 1997]. The N-S shortening is driven by the oblique subduction of the Juan de Fuca plate under the North American plate [*Riddihough*, 1984]. As a result, Cascadia is being squeezed between the Sierra Nevada block and western Canada [*Wells and Simpson*, 2001; *Wells et al.*, 1998].

The Seattle Basin is described in a litany of papers [*Blakely et al.*, 2002; *Brocher et al.*, 2001; *Pratt et al.*, 1997; *ten Brink et al.*, 2006; *ten Brink et al.*, 2002]. The nearby Tacoma Basin [*Brocher et al.*, 2001; *Pratt et al.*, 1997] and Everett Basin [*Johnson et al.*, 1996] have also been studied, but remain less well understood. The Kingston Arch separates the Seattle Basin from the Everett Basin, and the Seattle Uplift separates the Seattle Basin from the Tacoma Basin. In a series of studies, models were developed for these basins because the basins are known to amplify seismic shaking and many of the their buildings were constructed before knowledge of the severity of earthquake hazards [*Barberopoulou et al.*, 2004; *Frankel et al.*, 2002; *Frankel et al.*, 1999; *Pratt et al.*, 2003a].

The basins of the Puget Lowland require study to improve modeling of three-dimensional features. The young unconsolidated deposits are a temporally and spatially complex stratigraphy of glacial outwash, till, lacustrine, and recessional deposits formed when the Lowland was glaciated at least six different times in the Pleistocene [*Booth*, 1994]. The top several kilometers are peppered with smaller-scale basins and the deeper basins are likely delineated by the major bounding faults.

Seismic Hazards

Three types of earthquakes periodically occur in the Seattle area, as is typical for subduction zones:

(1) Most damaging for the urbanized areas are the shallow crustal events [*Haugerud et al.*, 2003; *Sherrod et al.*, 2004; *ten Brink et al.*, 2002] due in part to their close proximity. The most recent documented instance of a large event on the Seattle fault was the M7.2 event in about 900AD [*ten Brink et al.*, 2006], which featured 7m of surface slip, landslides, and a downtown Seattle seiche. There is also evidence of uplift in the vicinity of the Tacoma Fault about 1000 years ago [*Brocher et al.*, 2001]. Numerous other faults are present, and more are being found as geologists image the landscape with Light Detection And Ranging (LIDAR), but which faults are currently active and their recurrence intervals are not well known.

(2) M9 events strike the Cascadia coast roughly every 500 years [*Atwater*, 1992; *Goldfinger et al.*, 2003; *Satake et al.*, 2003]. These events produce strong long-period basin excitation lasting many minutes. The frequency and distribution of M8 events along the subduction zone is largely unknown.

(3) Flexure within the subducting slab has been the most common cause of strong earthquakes in recent decades, with M6.5 to M7 events in 1949, 1965, and 2001.

Seismic hazards are commonly estimated by predicting the shaking at a hard rock site from vertically incident seismic waves using a regional velocity model, then applying an amplification factor for non-hard rock sites that account for the effects of loose, unconsolidated sediments. However, the basins have an additional effect of focusing and trapping energy within them [*Frankel et al.*, 2002; *Frankel et al.*, 2007], which is not modeled with many traditional methods.

Some of the patterns of shaking have been captured with studies solely examining site amplification [*Hartzell et al.*, 2000]. Those results, however, are difficult to extrapolate to the sites for which recordings have not been analyzed, and to the many sites for which back-azimuth to an earthquake has a strong influence on the motions. Recorded ground motions from both strong and weak shaking indicate patterns of amplification that vary with site location, source location, and frequency [*Barberopoulou et al.*, 2004; *Frankel et al.*, 2002].

Previous Models

Earthquake tomography has revealed the larger-scale features of the crust around Seattle [*Lees and Crosson*, 1990; *Pitarka et al.*, 2004; *Pratt et al.*, 1997; *Symons and Crosson*, 1997]. These studies find a crustal thickness of 35 km [*Schultz and Crosson*, 1996], and provide a useful regional velocity model as a starting point for basin models, but do not have adequate resolution to model basin waves. Also, because they were mostly derived from short-period, vertical-component seismometers, S-waves are difficult to reliably identify, and thus S-wave models are less well constrained.

High-resolution basin models have been solely built on P-wave observations until the most recent work [*Snelson et al.*, 2007], and even this model is only a two-dimensional cross-section. Most of the larger-scale S-wave velocity models are derived from the conversion of a P-wave velocity model through an assumed Poisson's ratio. Fluid content, porosity, and composition all affect Poisson's ratio, so a direct measurement of S-wave velocities is preferable. Tomographic models indicate a basin structure that has a symmetrical bowl shape in the E-W direction and asymmetry in the N-S direction consistent with formation by motion of the Seattle Fault.

Important details remain unresolved [*Snelson et al.*, 2007]. Estimates of the thickness of the unconsolidated layers among recent models vary by up to a factor of two, begging resolution. The inference of several shallow sub-basins would benefit from verification and further study. Attenuation, a critical parameter for estimates of ground shaking, has only been estimated from active source experiments [*Li et al.*, 2006]. There are several different hypotheses for why the largest amplification occurs at stations above the deepest part of the Seattle Basin, such as focusing of teleseismic energy by the serpentinized upper mantle, or that the observed amplification is primarily controlled by unconsolidated sediments [*Pratt et al.*, 2003a].

Data

Most of my data came from the Seattle SHIPS array [*Pratt et al.*, 2003b] with some additional data from stations around Seattle from the PNSN and TA (Figure A2). During the Seattle SHIPS experiment, seismometers were deployed at 87 sites in a 110-km-long east-west line, three north-south lines, and a grid throughout the Seattle urban area from January to May 2002. Each site recorded three-components of velocity using a 2-Hz L-22 sensor recording 50 samples per second. The PNSN and TA sites had three-component broadband Streckeisen STS-2, Guralp CMG-40T, or Guralp CMG-3T sensors recording 40 samples per second.

The L-22 sensor is a short-period instrument. However, I was able to determine Rayleigh wave group velocities out to periods 10 seconds or more in many cases by careful selection and processing of the data. Each instrument was individually calibrated during the

SHIPS experiment and I used the individual calibrations to deconvolve the instrument response, eliminating most of the variability in response among the instruments. According to the calibrations, the velocity sensitivity was on the order of 100 times higher at a period of one second than at a period of 10 seconds. Still, the amplitude of coherent energy at a period of 10 seconds was often high enough to observe a good Rayleigh wave signal. I whitened the spectrum before band pass filtering to ensure the proper frequency content in each wavelet despite frequency-dependent instrument sensitivity.

To extract Rayleigh wave wavelets, the vertical-component seismograms from all stations were merged then cut to daylong segments. The instrument response was deconvolved; the signal was integrated to displacement, and the data down-sampled to 10 samples per second. The cross-correlations were computed as in Bensen *et al.,* [2007]. I used one-bit amplitude normalization because it produced cleaner and more prominent Rayleigh wave wavelets than other amplitude normalization methods. Some station pairs were discarded if the inter-station distance was not sufficiently large relative to the wavelength of the surface wave. Though I did not use a specific distance cut-off, I used only well-formed surface wave wavelets. I used an automated system to discard the worst traces and manually evaluated the rest. Due to my selectivity in picking only the best data, I used only 13% of the possible paths.

I first calculated the group velocity dispersion curve of each trace, starting at the longest period available, by calculating and selecting the peak of the envelope function. When I could not obtain the group velocity dispersion up to a period of 20 seconds, which occurred in most of the paths, I extrapolated the curve by using group velocity measurements calculated from the velocity model of Stephenson [2007]. By applying a band pass filter in small increments to my waveforms, I was able to track the peak of the envelope function to shorter periods, often down to between 2 and 3 seconds. I terminated my group velocity curve when the signal-to-noise ratio fell below 11.5 dB, or if the peak of the envelope function jumped, split, or was otherwise ambiguous to track. An automated evaluation process selected promising dispersion curves, which I visually inspected to discard additional station pairs. The paths used are shown in Figure A3.

As described in Bensen *et al.,* [2007], an additional constraint was needed to resolve the phase ambiguity associated with the calculation of surface wave phase velocities from group velocities. To solve this ambiguity I calculated Rayleigh wave phase velocity dispersion curves for a uniform grid of 1-D profiles taken from the shear wave velocity model of Stephenson [2007], using the method of Takeuchi and Saito [1972]. Throughout the model, the calculated phase velocity dispersion curves converge to ~3.91 km/s at a period of 20 seconds indicating a nearly 1-D velocity structure beneath the Seattle Basin (depths below 9 km). Calculated phase velocities ranged from 1 to 2.25 km/s at a period of 1 second indicating that velocities at basin depths vary laterally. I assumed that the Rayleigh wave phase velocity is 3.91 km/s at a period of 20 seconds everywhere beneath the Seattle Basin and integrated the group velocity curve from 20 seconds down to 2 seconds to determine phase velocities at these shorter periods. The group velocity curve between 20 and 10 seconds was based on a combination of values from the model of Stephenson [2007] and from my cross-correlations. The group velocity curve between 10 and 2 seconds was based exclusively on my cross-correlations. In this fashion, I resolved the phase ambiguity and calculated the phase velocity dispersion curve from the group velocity dispersion curve using the phase velocity at a period of 20 seconds as the constant of integration:

$$S_c(\omega) = \omega^{-1}\left(\int_{\omega_n}^{\omega} s_u(\omega)d\omega + \omega_n s_c^n\right),$$

in which s_u is the group slowness, s_c is the phase slowness and the "n" indicates a period of 20 seconds [*Bensen et al.*, 2007].

In order to test the resolving power of the paths shown in Figure A3, I ran a resolution test (Figure A4). In this test I generated a synthetic model based on my starting model, but with a checkerboard of velocity perturbations with a magnitude plus or minus 5%. In the central basin, each element of the checkerboard has a width and height of 7 km. The results show that the essential features of the staring model are resolved in the central part of the basin where data coverage is the best.

Model Calculation

I calculated the 3-D shear wave velocity model in two steps. In the first step, I solved for the 2-D Rayleigh wave phase velocity model as a function of period between 2 and 10 seconds. The model space is 110 km east to west and 145 km north to south, centered on Seattle. The velocity model was parameterized with an irregularly spaced grid, with smaller spacing in regions with greater data coverage. Inter-grid spacing ranged from 1 km near central Seattle to 20 km at the edges of the model. At each grid point, I used a 3rd order polynomial for phase velocity as a function of frequency. At each frequency and grid point, I calculated a Gaussian surface with a characteristic width equal to the square of the distance to the next closest grid point. The normalized sum of these surfaces determined the 2-D velocity model at each frequency. I used a starting model from Stephenson [2007] and two different forward calculations, ray theory and a single-scatterer approximation, to calculate the polynomial coefficients.

I inverted for the polynomial coefficients of the model using the following equation:

$$\underline{m} = \left(\underline{\underline{G}}^T \underline{\underline{C}}^{-1} \underline{\underline{G}} + \gamma^2 \underline{\underline{L}}^T \underline{\underline{L}}\right)^{-1} \underline{\underline{G}}^T \underline{\underline{C}}^{-1} \underline{d}$$

C is the data covariance matrix. *G* is the partial derivative matrix. *L* is the normalization matrix described below. γ is a scaling parameter between goodness of fit and the normalization matrix. *d* is the data vector of observed phase velocities and *m* is the model vector of polynomial coefficients.

In determining the data uncertainties for matrix C I estimated the uncertainties in calculating the Rayleigh wave phase velocities. The most important source of error in my phase velocity calculation was the way I augmented my dataset and solved the phase ambiguity using the model of Stephenson [2007]. To test the error that would be introduced if my assumption that the phase velocity is 3.91 km/s at 20 seconds everywhere in the model was incorrect, I considered other values. If I was off the actual phase velocity by 5% at a period of 20 seconds, the error introduced would only be about 2% at a period of 2 seconds, less for periods between 2 and 10 seconds. Another source of error comes from the possibility of phase shifting in the empirical Green's functions if the azimuthal distribution of coherent noise at the periods I used was highly focused, though I did not find that to be the case. It was difficult to know for sure how much error is present, so I used a conservative estimate of 10% in my inversion.

The normalization matrix (*L*) is the sum of two different matrices. The first matrix is a diagonal matrix whose values were determined by the geographic location of the corresponding parameter. For each grid point, I calculated its mean distance to all of the stations which is used as a proxy for the relative amount of data coverage at the grid point. If a grid point was near many stations, its mean distance would be small and therefore the data coverage high. For points with a low mean distance I gave a lower variance and for stations with a high mean distance I give a higher variance. In this way I was able to discourage parts of the model with sparse data coverage from drifting very far from the starting model and simultaneously emphasize perturbations calculated for the parts of the model with a high density of observations. The second matrix measured the geographic roughness in the model using a finite difference approximation of the curvature. With this matrix I was able to apply a penalty for increasing roughness.

In order to estimate the effect of the starting model on my results, I ran this inversion using many different starting models. Beginning with my basic starting model, I added Gaussian noise with a standard deviation of 20% to all model nodes within the basin. I ran each of these models to a solution then calculated the mean and standard deviation of the results. Within the basin, most regions showed a standard deviation of much less than 10%, with a few isolated spots as high as 15% where data coverage was sparse. This indicated that there is some dependence on the starting model mostly in the shallowest layers, but the variations were within my estimated uncertainties.

In the second step, I inverted the Rayleigh wave dispersion curves for the 3-D isotropic shear wave velocity structure. The horizontal dimensions are 60x60 km, centered on Seattle with uniform horizontal grid spacing of 2.5 km. The phase velocity model was bigger than the shear wave velocity model in order to include several stations outside the basin. However, for the shear wave velocity inversion, it was no longer necessary that those stations lie within the model so I omitted parts of the model with the poorest data coverage. The vertical extent of the model was 160 km in depth in order to avoid any boundary problems with the forward problem, however the Rayleigh wave frequencies I estimate were most sensitive to the top ~4 km of the model. Between 4 and 9 km depths, velocities were highly smoothed in part because I assigned higher penalties for roughness and deviation from the starting model at these depths and below. The grid spacing in the upper 10 km of the model ranged from 0.25 km to 1 km and the spacing size increases with depth through the rest of the model. I considered inclusion of a water layer for Puget Sound and Lake Washington, but at periods of 2 seconds and greater, the effect of the water layer for the relevant depths was only about 1 percent and only in very localized places.

I used a starting model based on Stephenson [2007] and calculated synthetic dispersions curves in my forward calculation using the method of Takeuchi and Saito [1972]. I used a full 3-D inversion so that I could apply normalization to the model as a whole. My shear wave velocity inversion was similar to my phase velocity inversion described above. I used two normalization matrices: one was a Laplacian matrix that is designed to apply a penalty for increasing roughness, and the other was a parameter variance matrix that allows us to hold steady model parameters that were in regions not well constrained by the data while allowing other parameters to vary more freely. In particular, I assigned high variances to parameters deeper than 9 km since that is below the bottom of the Seattle Basin, where I had little constraints from my data. As in the first inversion, I calculated solutions from a number of starting models perturbed by adding Gaussian noise to my original starting model. This time, the standard deviation of the noise was 5% and the same noise is added to all points in a column. I used smaller levels of noise than with my phase velocity calculations because adding higher levels of noise could have led to the generation of physically unrealistic velocity structures, which caused problems with the forward calculations. The resulting suite of models has a standard deviation of only about one percent except in the uppermost layer.

Results

I extracted Rayleigh waves from the vertical components of the SHIPS array using noise interferometry. Four representative examples of station pairs are shown in Figure A5. The relative amplitudes of the acausal and causal signals indicate that the sources of coherent noise are well distributed in azimuth. The measured group velocities indicate that velocities for paths within the Seattle Basin are slower than paths that are outside of the Seattle Basin.

My Rayleigh wave phase velocity results show a clear low velocity zone that is consistent with the area of low residual isostatic residual gravity shown in Figure A1, measuring ~60 km from east to west and ~45 km from north to south (Figure A6). The lowest velocities at all periods are near downtown Seattle, just to the north of the Seattle fault. Rayleigh waves with periods between 2 and 6 seconds are sensitive to the upper 5 km in this setting and those with periods between 8 and 10 seconds are sensitive to the depth range 5-15 km. At a period of 2 seconds the velocities are as low as ~625 km/s, and the lowest velocities at a period of 10 seconds are 960 km/s. With increasing period, the apparent diameter of the basin shrinks. Potential sub-basins are revealed in the southwest, north, and east. There is less apparent structure in the deeper parts of the basin. However, due to the broadening sensitivity kernels of Rayleigh waves at longer periods, it is also more difficult to resolve smaller structures with 8 to 10 second waves.

My shear wave velocity results show that velocities are slower in some areas in the top 1.5 km of the Seattle Basin beneath the city of Seattle than in the model of Stephenson [2007] (Figure A7). Additional images of my model are included as an electronic supplement. My dataset does not uniquely constrain the uppermost ~250 m of the basin, but by using a 1-D average from the model of Stephenson [2007] as my starting model, I inherit the ~600 km/s velocities in the uppermost layers from that model. By using different plausible starting models, the uppermost layer could be anywhere from 400-750 m/s according to my calculations. Below 500m, my calculations show little dependence on the starting model. Beneath the uppermost layers I found low velocities persist to at least 3 km, where my velocities were lowest just north of the Seattle Fault with lesser amounts in other parts of the basin. Below 3 km my results show velocities approaching those of Stephenson [2007].

I compared the constant velocity contours in the 2-D refraction profile of Snelson *et al.,* [2007], that runs west to east across the Seattle Basin, to the same contours from my new model. There are small-scale differences at all depths. However, both models put the 2 km/s shear wave velocity contour at depths between 3-4 km across the central part of the basin. The main difference between the two models is that my 1.0 km/s and 1.5 km/s contours are closer to the surface. For the Snelson *et al.,* [2007] model, the depths are approximately 1 and 2 km, respectively. In my new model, the depths are approximately 0.5 and 1.5 km, respectively. In the model of Snelson *et al.,* [2007], velocities are slightly slower to the west of Puget Sound than to the east and my velocities are slower to the east of Puget Sound then to the west in the upper 3-4 km.

Model Validation

I assessed my new model's ability to predict amplitudes relative the model of Stephenson [2007] because it was used in the development of Seattle's seismic hazard maps. For all of my amplitude comparisons I calculated waveform envelopes. I calculated peak motions in a window that starts just before the direct shear wave arrival and ends after the direct surface wave arrival, and then I took the geometric mean of the two horizontal components to capture both Love and Rayleigh waves. I used periods between 1-2 seconds because this is the band in which most buildings and transportation infrastructure are vulnerable and because in this band is where I expected the most differences between the two models.

Frankel [2009] showed a good phase match between data and synthetics for the 2001 Nisqually 6.8 event in the 0.2-0.4 Hz band using the Stephenson [2007] model. I expected and produced very similar results in this band using my local model embedded in the Stephenson [2007] regional model because waves in this band are not strongly affected by my updates to shallow structure from my tomography results. At shorter periods addressed in this study, I neither expected nor achieved a good phase match between synthetics and data. I based my validation on the arrivals and amplitudes of the shear and surface waves.

In Figure A8 I show a data and synthetic to demonstrate what I considered a well-fitting prediction. Many of the urban strong motion sensors used in this study are by necessity located in noisy locations. Even though there is some noise in the data, the shear wave and surface wave arrivals on the horizontal components are very close in arrival time and amplitude despite a phase mismatch. On the north component, the synthetic shear wave has higher amplitude than the data, but on the east component that relationship is reversed. These differences could be the result of an issue with the modeled radiation pattern or unmodeled anisotropy, as well as small inaccuracies in velocity model. Since I use the mean of both horizontal components and because the well-fitting surface wave controls the maximum amplitude in this example, it yields an excellent match. In addition, the amplitude of the coda is similar throughout this fifty-second trace even though I didn't consider the coda in my evaluation. In some other examples one of the horizontal components fits well while the other one does not, or the arrival times are shifted slightly. Unmodeled scattering, focusing and/or multipathing could explain some of these amplitude, phase, or arrival mismatches.

To evaluate the predictive ability of the two velocity models, I selected two unmodeled local events that were widely recorded by strong motion stations in the Seattle area, many of which were recently deployed. The first event, referred hereafter as the Carnation event, had a magnitude of 3.4 and occurred on May 25, 2010 at 47.679N, -121.978W (28 km east of Seattle), at a depth of 6 km (Figure A9). This is a shallow crustal event with a hypocenter within the North American plate. The second event, referred hereafter as the Kingston event, had a magnitude of 4.5 and occurred on January 30, 2009 at 47.772N, 122.557W (25 km northwest of Seattle) at a depth of 58 km (Figure A10). This is a Benioff Zone event with a hypocenter located within the subducting Juan de Fuca plate. I used the finite-difference code of Liu and Archuleta [2002] to simulate these two earthquakes for comparison with the recorded data.

Since neither of the two local events have a hypocenter that is within my new model, I embedded my new model into the regional model of Stephenson [2007], which encompasses both hypocenter locations. I extracted the upper 3.5 km of my new model, and pasted it into the model of Stephenson [2007]. I applied some averaging near the suture between the two models to avoid discontinuities, and then explicitly added a discontinuity to represent the Seattle fault. This fault discontinuity follows the frontal surface trace described by Blakely [2002], is dipping 45 degrees to the south, and is given a 10% velocity contrast that decays exponentially away from the fault surface.

Vertically propagating shear waves at periods above 3 seconds in a medium with velocities between 600-1500 m/s will not be strongly affected by a 3.5 km thick region, the maximum depth of my new velocity model within the regional velocity model. Body and surface waves at periods between 1-2 seconds can be strongly affected by a 3.5 km thick region. I expect and observe that long period (>3 s) arrivals calculated using the two models to be very similar to one another in phase and amplitude, while shorter period waves are sometimes different.

The Carnation event was recorded on 27 stations located on stiff soil sites as shown in Figure A9a. For 15 of these stations, amplitudes for periods between 1-2 seconds calculated using my new model are closer to the data by more than 5% compared to amplitudes using the previous model. For 2 of these stations, there is less than 5% difference between the two models. For 10 stations, the previous model yields better amplitudes by more than 5%. I also averaged the misfit across all stations at different frequencies between 0.5-1 Hz (Figure A9b). I calculated the points on this figure by first dividing the synthetic amplitude by the data amplitude. Then I subtract one from the absolute value of the mean ratio for each station so that a value of zero indicates a perfect match in amplitude. Average amplitudes calculated using my new model are closer to the data than those calculated using the previous model at all frequencies in the range. Even though the previous model makes better predictions at some stations, the difference between the two models tends to be smaller at those stations than for stations where my new model does better, which is evident in the averages shown in Figure A9b.

In Figures A9c and A9d, I show a scatter plot of all of the amplitudes that are averaged to make Figure A9b. There is a significant amount of scatter that could represent either site effects from unconsolidated sediments or unmodeled structure. As a local crustal event, the seismic waves traveling from the hypocenter to each station travels ~20 km through heterogeneous upper crust. I will see that the Kingston event, a Benioff Zone earthquake, has a much tighter scatter plot due to smaller path effects.

In addition to the complications due to path effects there is some uncertainty in the moment magnitude for the Carnation event. The PNSN catalog states this event has an M_d of 3.4. Using a moment magnitude of 3.4 results in the amplitudes of the synthetics systematically overestimating the amplitudes of the data using both models. I found that simulating this event with a moment magnitude of 3.25 resulted in the best overall fit with the data, but the previous model still has a greater tendency to overestimate the amplitudes. Amplitudes calculated with my new model are more closely clustered around the observed amplitudes, especially at longer periods in the range considered.

The Kingston event was recorded by 23 stations located on stiff soil sites as shown in Figure A10a. For 12 of these stations, amplitudes calculated using my new model are closer to the data by more than 5% compared to amplitudes using the previous model. For 8 of these stations, there is less than 5% difference between the two models. For 3 stations, the previous model yields better amplitudes by more than 5%. I also averaged the misfit across all stations at different frequencies between 0.5-1 Hz (Figure A10b). Between periods of 1.0-1.67 seconds my new model has amplitudes closer to the data, while the previous model has better amplitudes between 1.67-2.0 seconds. Compared to the Carnation event, synthetic amplitudes are closer to data amplitudes for both models, however my new model makes better predictions at most of the individual stations. The scatter plots shown in Figures 10c and 10d show that amplitudes calculated using my new model are more clustered around the observed amplitudes.

Interpretation

Due to the density of stations in the city of Seattle, I was able to resolve smaller features in the velocity structure than previous basin-wide models. As noted above, there is a pronounced low velocity zone just north of the Seattle Fault in Elliot Bay at the outlet of the Duwamish River, which is most evident, a 1 km depth. Basin sediments have lower velocities than the mostly crystalline rock to the south and north and I am able to resolve this contrast. To the west across Puget Sound, the fault trace shifts northward [*Blakely et al.*, 2002] which can be seen in my model at depths from 1-3 km. My data do not cover the entire length of the Seattle fault, but in places where I have data coverage I observed the associated velocity contrast. Velocity variations within the basin reveal several sub-basins that could have at least two different origins. Deeper sub-basins are likely formed by the evolution of the basin through a combination of thrust and strike-slip tectonic motions while shallower sub-basins are likely the result of glacial action including uneven compaction, deposition, and erosion.

Conclusions

I use ambient noise to directly observe the shear wave velocity structure of the Seattle Basin. The 3D structure of deep crustal basins has a significant impact on the propagation of seismic waves and seismic hazards in the cities that sit atop them. My shear wave model of the Seattle Basin contains more detail than the previous model used in seismic hazard assessments and may help explain some of the unmodeled amplitude scattering observed in previous efforts. I have shown quantitatively that my new model makes better predictions than the previous model for two local earthquakes.

My method's strength is the resolving power of short period Rayleigh waves on shear wave velocity in the upper few kilometers without the need to precisely know Poisson's ratio. My method's weaknesses are the inability to precisely resolve sharp discontinuities and uniquely constrain velocities in the top 30-100 m. Resolving sharp discontinuities is better suited to reflection techniques. Determining amplification factors due to shallow, unconsolidated sediment is better suited to observations of strong motions and more local or point measurements of sediment thicknesses and shear wave velocity. I believe that my new model can be applied to predict levels of ground shaking with greater accuracy than the current seismic hazard maps for Seattle, as demonstrated by the two events I examined, due to more accurate modeling of shear wave velocities in the upper 3-4 km of the basin. I believe that most of the remaining misfit is likely due to site effects, sharp discontinuities not resolved by the tomography, and unmodeled structure from outside of my data coverage.

Further improvements in the Seattle Basin velocity model could be achieved using a more optimal station arrangement, more broadband instruments, a longer recording duration, and developing a joint inversion that explicitly includes geological information about sharp discontinuities such as faults and basin edges. However, using a limited, legacy dataset I was able to make measurable improvements to amplitude predictions for two local earthquakes at frequencies relevant to seismic hazard assessments.

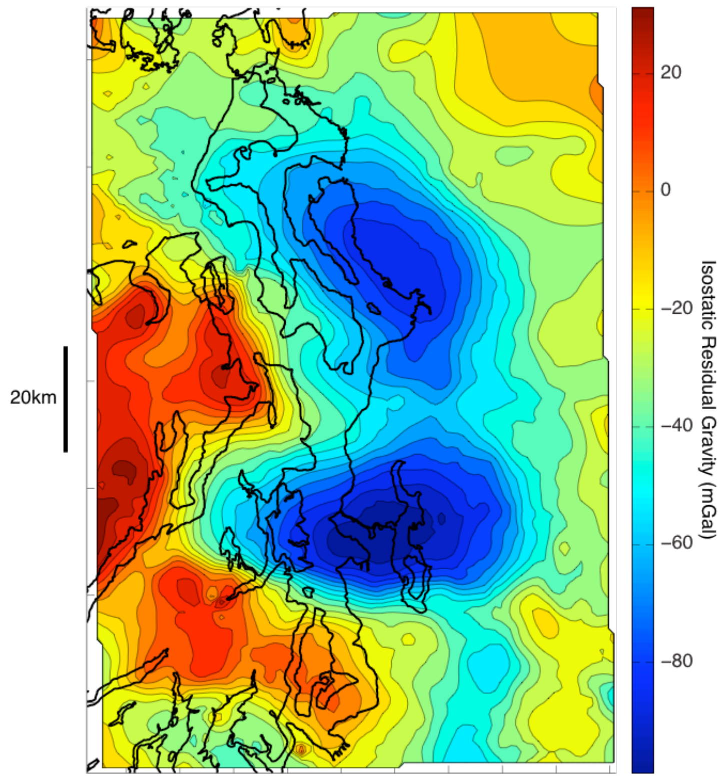

Figure A 1. Isostatic Gravity

Shown are the geometry of basins as revealed by gravity variations around Seattle, Everett, and Tacoma, Washington [*Brocher et al.*, 2001].

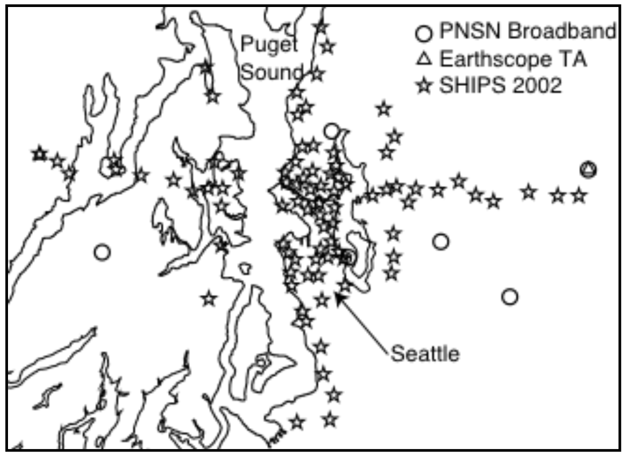

Figure A 2. Station Locations

Shown are the stations used for this study. The black curves indicate the coastline of Puget Sound and Seattle is located where stations are clustered in the center of the figure. Circles indicate broadband stations of the PNSN, triangles indicate broadband stations of the Earthscope's TA, and starts indicate stations of the SHIPS 2002 array.

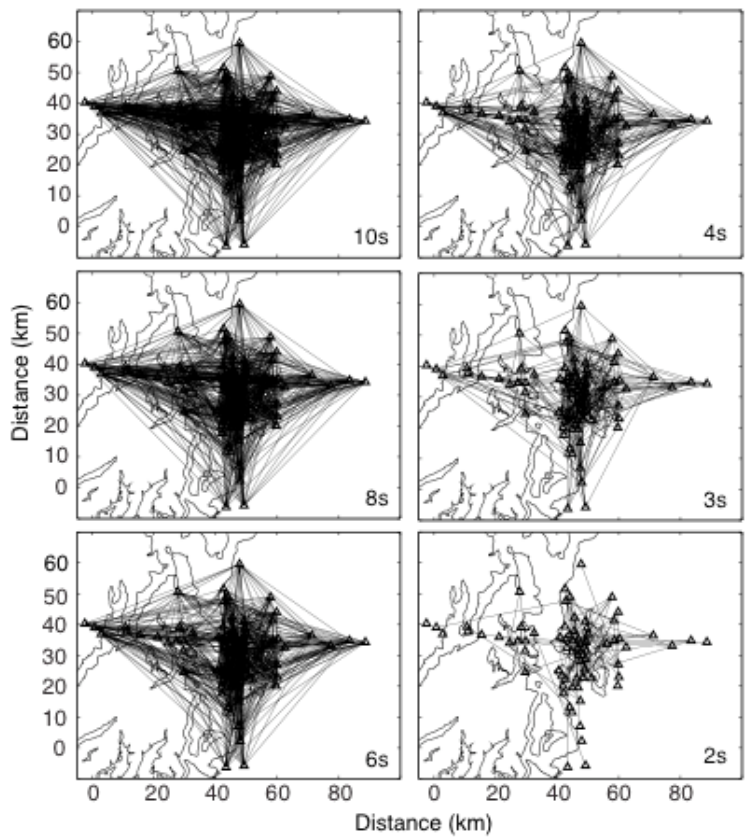

Figure A 3. Inter-station paths

Lines represent paths for Rayleigh Waves used to image the Seattle Basin. The period is indicated at the lower right of each subfigure. Triangles represent stations of the SHIPS array.

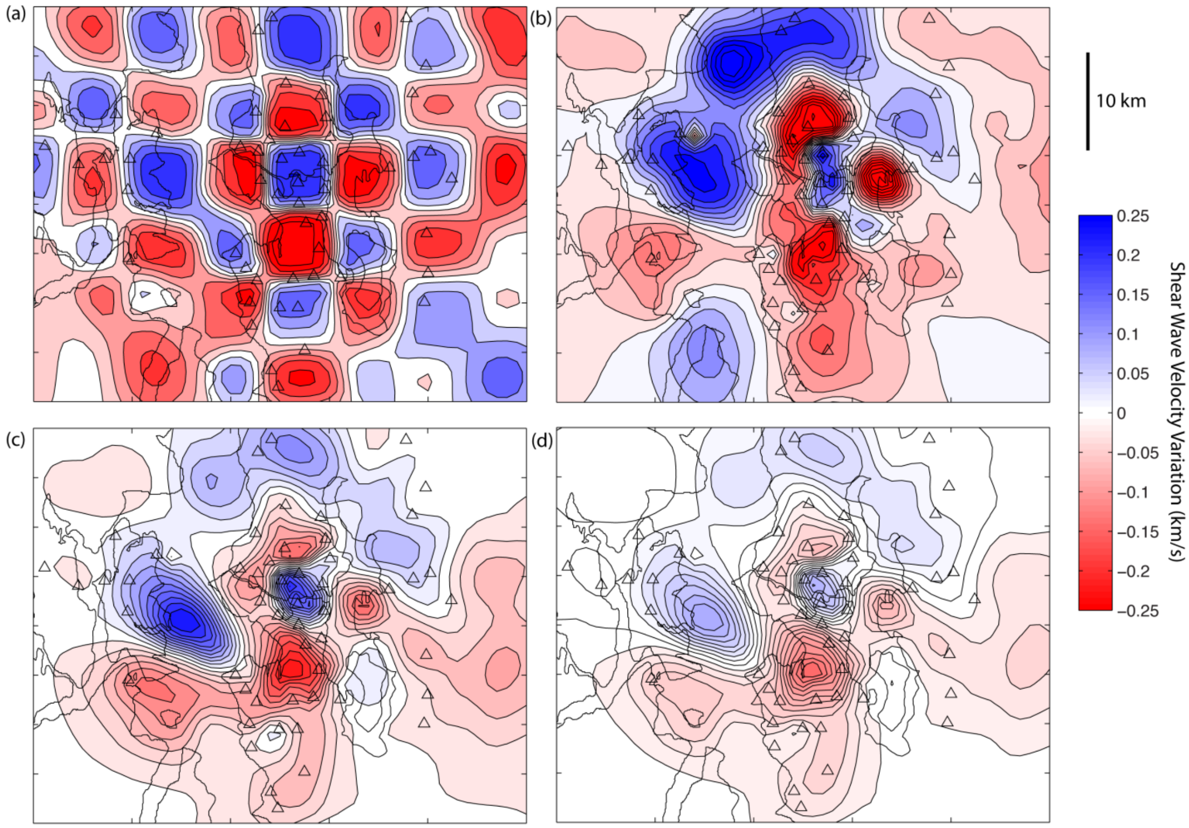

Figure A 4. Resolution Test

In (a) are the perturbations in a synthetic model. Each square is a maximum of plus or minus 5% from the mean. In (b), (c), and (d) are the results from an inversion for periods of 2, 3, and 4 seconds respectively.

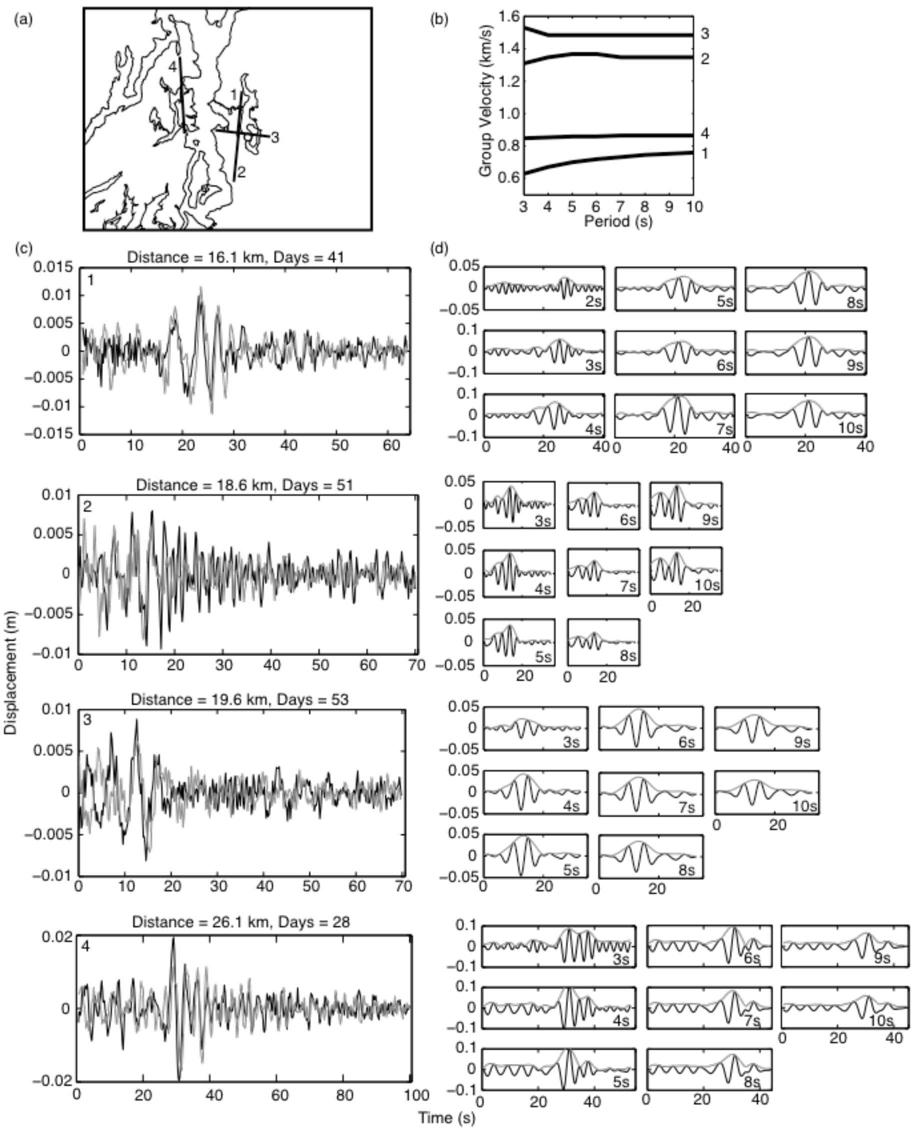

Figure A 5. Empirical Green's Functions

Shown are some number-coded examples of empirical Green's functions and Rayleigh wave group velocity measurements: (a) paths, (b) group velocity curves (c) empirical Green's functions (causal and acausal waveforms in gray and black) with station distance and recording duration, and (d) bandpassed waveforms.

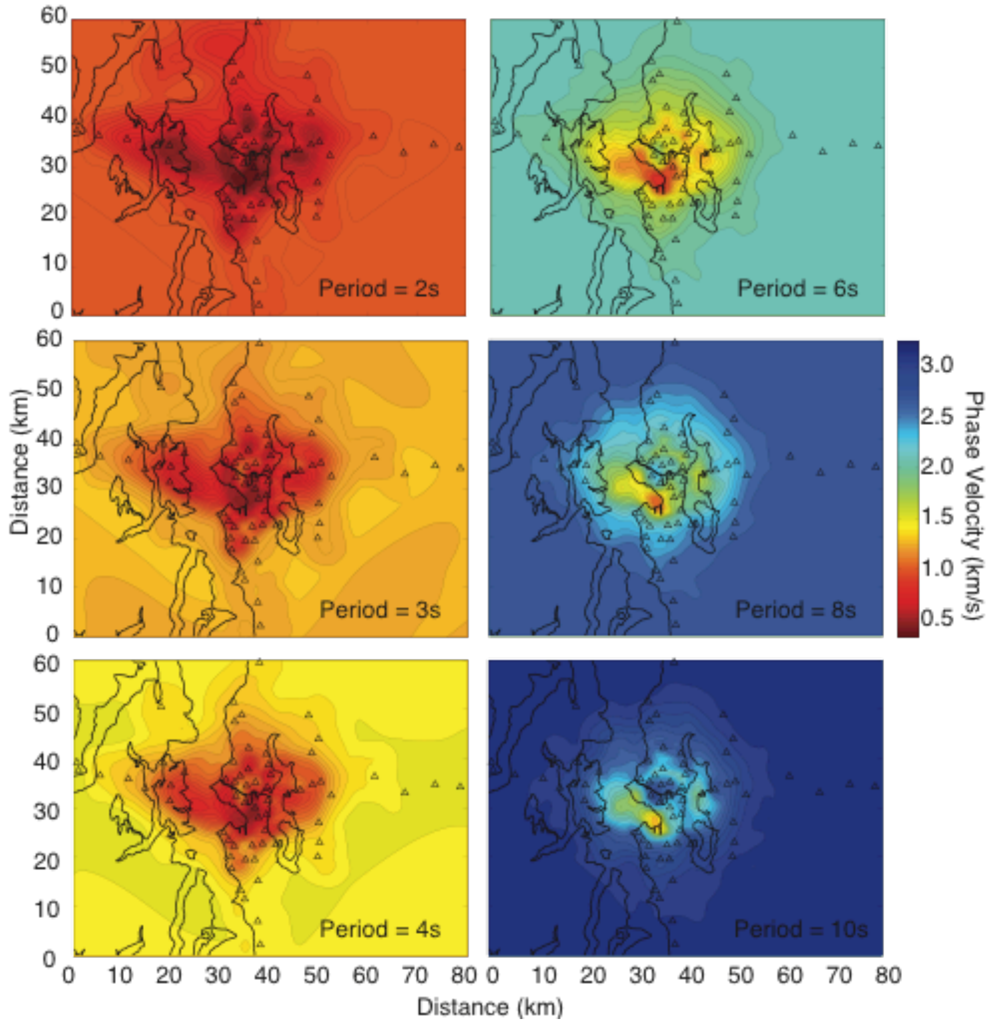

Figure A 6. Rayleigh Wave Phase Velocity

Shown are Rayleigh wave phase velocities for periods between 2 and 10 seconds. Black triangles represent stations of the SHIPS 2002 array.

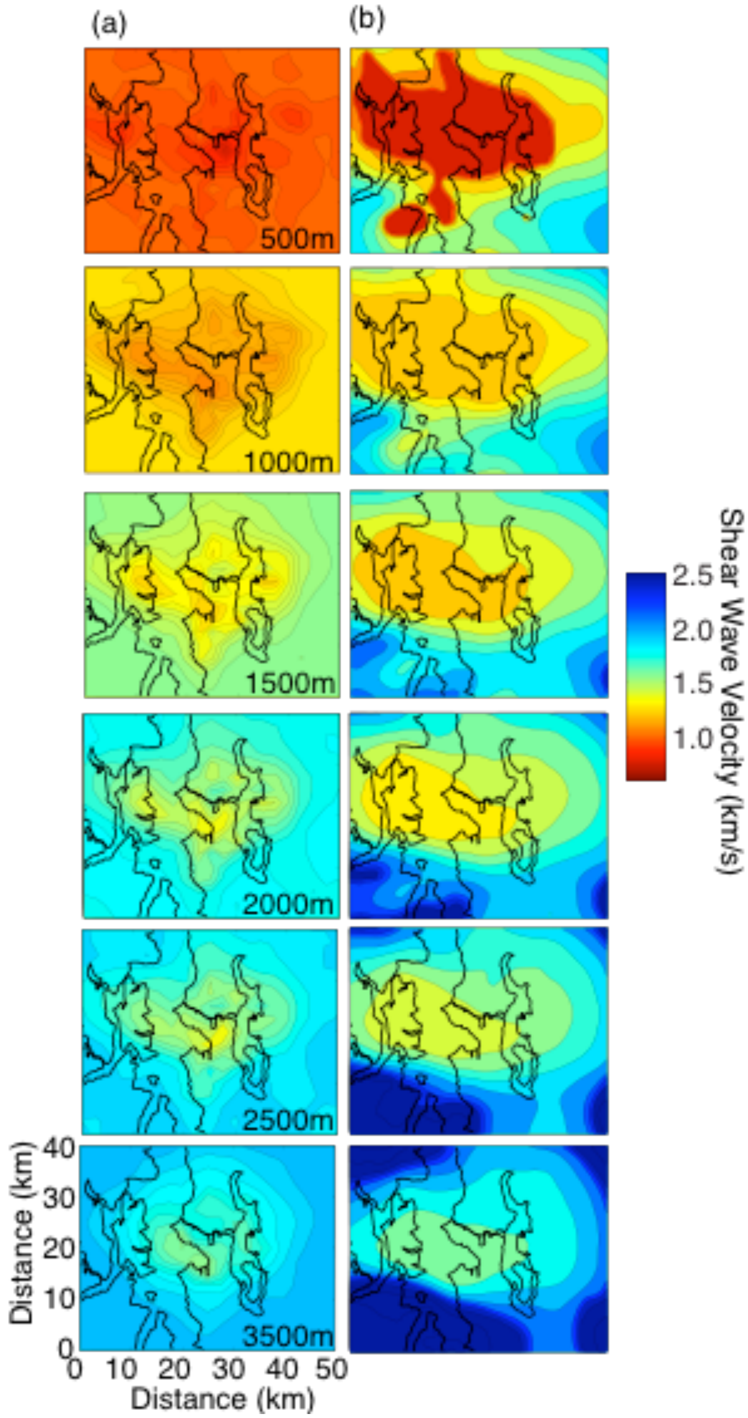

Figure A 7. Shear Wave Velocities

Shown is (a) my shear wave velocity model and (b) the model of Stephenson [2007]. Depths are indicated on each row. The coastline of Puget Sound is shown on each subfigure.

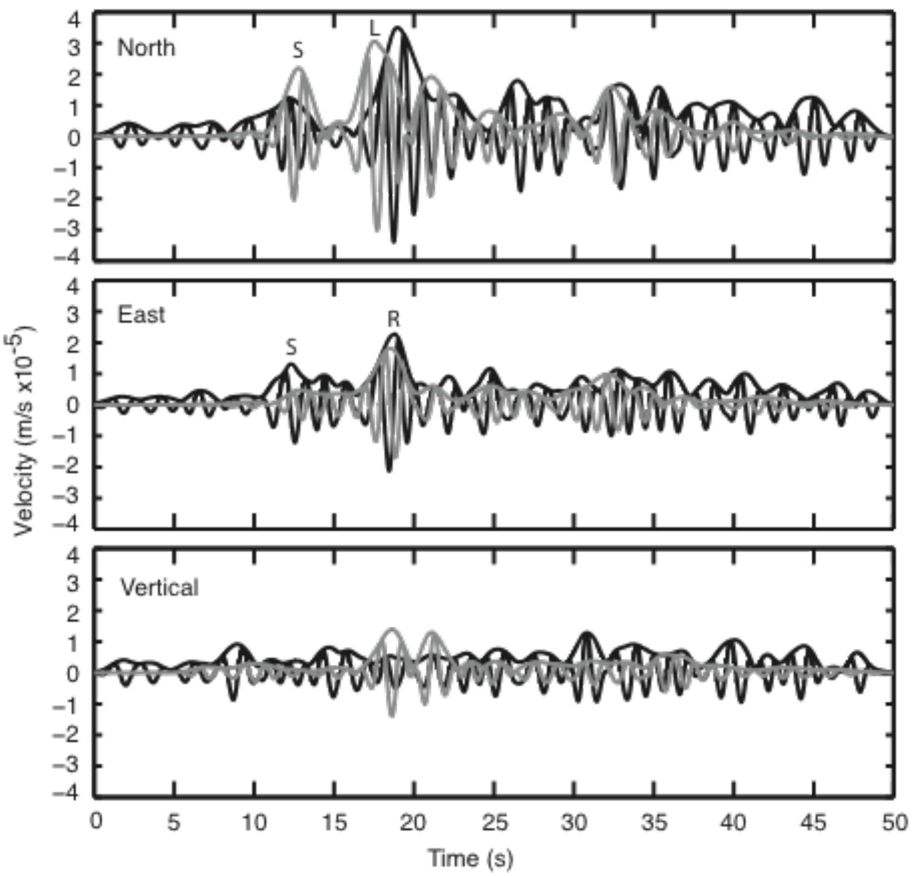

Figure A 8. Amplitude Comparison

Shown are data and synthetics of station QCOR for the Carnation event. Data are shown in black and synthetics are shown in gray. The shear, Love, and Rayleigh wave arrivals are denoted with “S”, “L”, and “R”, respectively. Traces are bandpass filtered with corner frequencies of 0.5-1 Hz.

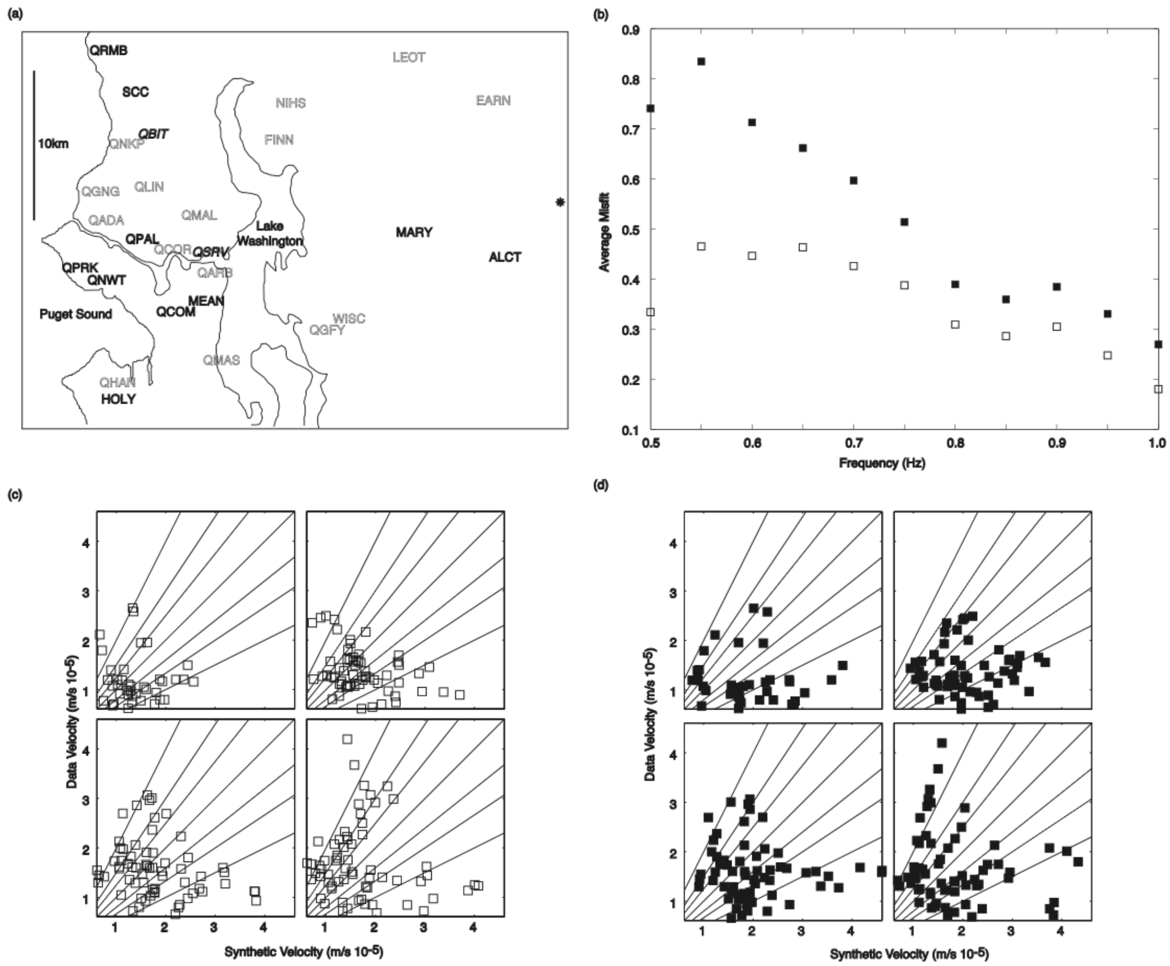

Figure A 9. Carnation event

(a) The asterisk indicates the event epicenter. Outlined station names indicate stations where my new model produces better amplitudes than the previous model. Bold station names indicate stations where the previous model produces better amplitudes than my new model. Italicized station names indicate stations where amplitudes produced by the two models are within 5%. (b) Shown is the average misfit as a function of frequency. Solid squares indicate amplitude misfit for the previous model and open squares indicate amplitude misfit for my new model. Scatter plot for amplitudes calculated from my new model (c) and the previous model (d) compared to the observed amplitudes, in four bins between 0.5-1 Hz, are shown from left to right then top to bottom. In these four axes, when a square is on the centerline with a slope of one, that indicates a perfect match of amplitudes between data and synthetic. The next line with a smaller slope indicates that the synthetic is 25% greater than the data. The next two lines with smaller slopes indicate 50% and 100% greater, respectively. The lines with a slope greater than one indicate 1/1.25, 1/1.5, and 1/2, respectively, with the data greater than the synthetic.

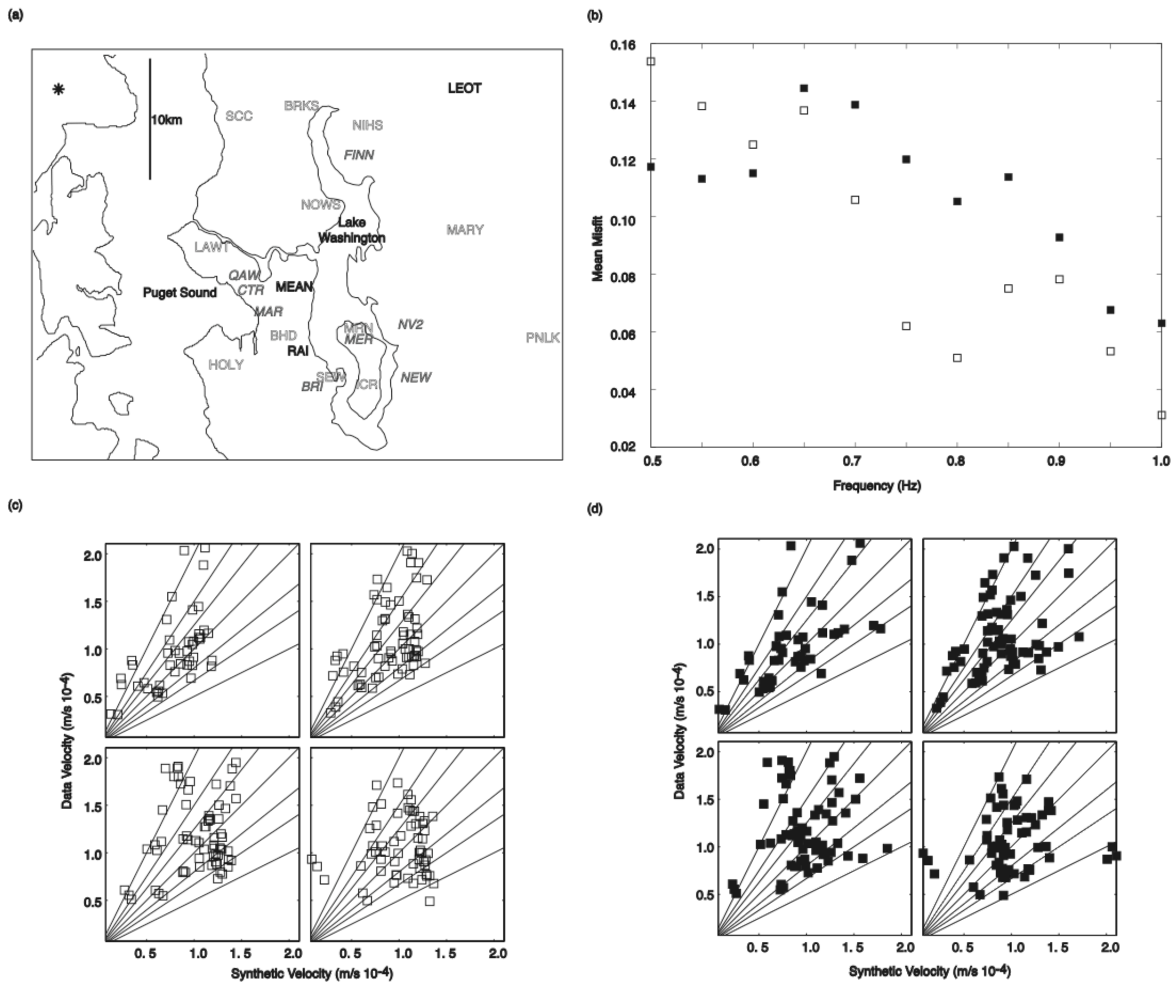

Figure A 10. Kingston Event

(a) The asterisk indicates the event epicenter. Outlined station names indicate stations where my new model produces better amplitudes than the previous model. Bold station names indicate stations where the previous model produces better amplitudes than my new model. Italicized station names indicate stations where amplitudes produced by the two models are within 5%. (b) Shown is the average misfit as a function of frequency. Solid squares indicate amplitude misfit for the previous model and open squares indicate amplitude misfit for my new model. Scatter plot for amplitudes calculated from my new model (c) and the previous model (d) compared to the observed amplitudes in four bins between 0.5-1 Hz, are shown from left to right then top to bottom. In these four axes, when a square is on the centerline with a slope of one, that indicates a perfect match of amplitudes between data and synthetic. The next line with a smaller slope indicates that the synthetic is 25% greater than the data. The next two lines with smaller slopes indicate 50% and 100% greater, respectively. The lines with a slope greater than one indicate 1/1.25, 1/1.5, and 1/2, respectively, with the data greater than the synthetic.

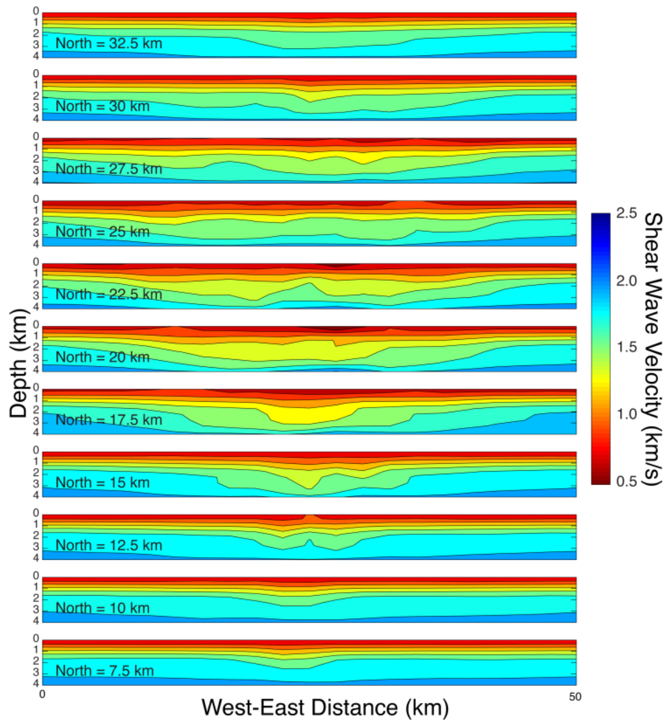

Figure A 11. West-East Model Cross-section

Shown are west to east vertical cross-sections of my shear wave velocity model. North and west-east distances correspond to the axis in Figure 6a.

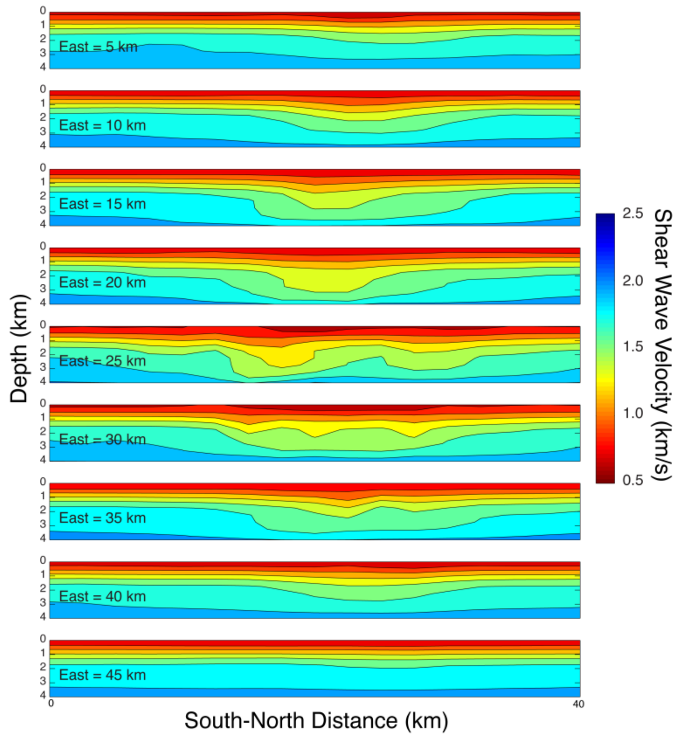

Figure A 12. North-South Model Cross-section

Shown are south to north vertical cross-sections of my shear wave velocity model. East and south-north distances correspond to the axis in Figure 6a.

Predicting Ground Motions

The purpose of predicting ground motions is to apply those predictions in a PSHA. The basic equation for a PSHA is shown below:

$$\lambda(u > u_0) = \sum_i \sum_j \sum_k \gamma_i P\big[u > u_0 | M = m_j, R = r_k\big] P\big[M = m_j\big] P[R = r_k]$$

In this equation *u* is the predicted ground motion. The value in the first set of brackets is the attenuation relationship, the probability that the predicted shaking will exceed some given level of shaking for a particular magnitude earthquake at a particular distance from the location of interest. This is multiplied by the value in the second set of brackets, the probability of having an earthquake of a particular magnitude, and multiplied again by the value in the third set of brackets, the probability of having an earthquake at a particular distance. Then I sum over all earthquakes (*i*), magnitudes (*j*), and locations (*k*) as indicated by the three summation symbols. To add the time dependence I use the following equation:

$$q = 1 - e^{-\lambda t}$$

In this equation *t* is the time duration and λ is from the PSHA equation above.

Ground shaking *u* itself can be broken up into several components:

$$u = u_{rock} A_{3D} A_{site} A_{non-linear}$$

In this equation u_{rock} is the level of shaking at the crystalline basement. This may be at the surface, or it may be many kilometers deep, depending on the geologic environment. In the case of the Seattle Basin, this can be as deep as 9 km. A_{3D} is the amplification due to the structure of the upper crust. In the case of the Seattle Basin, this is the amplification effect of the contrast between velocities of the basin sediments and surrounding rock as well as the structure within the basin. A_{site} is the amplification due to unconsolidated sediments, which could be anywhere from 0 to tens or hundreds of meters thick. $A_{non\text{-}linear}$ is amplification due to non-linear behavior in unconsolidated sediments. In most cases this value is less than one since accelerations generally decrease when sediments behave in a non-linear fashion.

In this study, I focus on A_{3D}, the amplification due to the velocity contrast between basin sediments and the surrounding rock. Using a new velocity model, I run simulations for Benioff Zone earthquakes in the Juan de Fuca Plate within around 50 km horizontal distance from Seattle as well as simulations for crustal events occurring at a variety of azimuths from Seattle. By comparing amplitudes inside the Seattle Basin to those outside the basin, I can make predictions for how the Seattle Basin amplifies incoming seismic waves.

In order to calculate a PSHA for Seattle, hundreds to thousands of events must be considered among the three earthquake categories: Cascadia megathrust, Juan de Fuca Benioff zone, and North American crustal events. Ideally, every possible event would be simulated uniquely. Due to computational limitations, Frankel *et al.,* [2007] selected a set of representative events to simulate in each of the three categories. Then, for each predicted event, they used the closest and most similar simulated event for ground motion predictions. The obvious limitation of this approach is that there is so much variety in azimuth, depth, and focal mechanism that some predicted events will not be well simulated within a limited set of representative events. The more comprehensive the set of representative events, the better the ground motion predictions will be. Nobody knows ahead of time how much a few kilometers in depth or horizontally, or several degrees rotation of the focal mechanism will affect predicted ground motions.

Some events may be modeled as a point source including all Benioff zone and many crustal events. Many of these events are sufficiently far enough away from Seattle such that the finite fault effects are minimal. Even so, a variety of focal mechanisms must be considered. For events on nearby faults, like the Seattle fault and South Whidbey Island fault, earthquake sources cannot be modeled as a point source. This is also the case for a Cascadia subduction zone event whose rupture length could be over 1000 km with a rupture of duration several minutes. In order to properly simulate earthquakes on such faults many different simulations need to be performed covering the range of possibilities for the size of and location of the fault patch, its rupture direction and pattern of asperities. Using a limited set of simulations would lead to predictions that are biased by the radiation pattern of the selected ruptures. By running hundreds of simulations using a wide range of plausible rupture scenarios we can avoid these biases.

I ran 17 different simulations to get an understanding of how the Seattle Basin affects the wave propagation from crustal and Benioff zone events (Figures B1 and B2). These simulations are made using the linear elastic code of Liu and Archuleta [2002]. The model is not fine enough in the upper tens of meters to simulate the effects of unconsolidated sediments. So, these results are predicting purely the effects of the upper crust on wave propagation. I selected 9 Benioff zone events and 8 crustal events. I use the same focal mechanism within each set of earthquakes. Seventeen simulations are not enough to calculate a PSHS. The purpose of this demonstration is to understand to the first order how the Seattle Basin affects wave propagation and to understand how azimuth and depth (for Benioff zone events) effect the predictions. The effect of the radiation pattern is not important for this demonstration because I do not make direct comparisons of the amplitudes between events.

All of the Benioff zone events use the moment and focal mechanism of the 2001 Nisqually 6.8 event which according to the PNSN, had a strike, dip, and rake of 349, 71, and -91 respectively. These events are placed at the appropriate depth for their epicenter according the depth of recorded events with similar epicenters in the PNSN earthquake catalog. All of the events are either west of Seattle or beneath. East of Seattle, the Juan de Fuca plate is deepest and dips more steeply, so any event in this area will generate essentially vertically propagating waves as they impinge on the Seattle Basin which is simulated by an event directly below Seattle.

For the 8 crustal events, I placed them each at the center of a 45 degree pie wedge, all at a depth of 10 km. Each event has the same focal mechanism with a strike, dip, and rake of 90, 45, and 90 respectively. This focal mechanism is similar to what I would expect for a rupture on the Seattle fault. All events have a moment magnitude of 6.5.

Peak horizontal ground velocities are shown in Figures B3, B4, B5, and B6. Each figure shows the average peak horizontal ground velocity for three simulations. Figure B3 shows the average velocities from the three most northern epicenters and Figures B4, B5, and B6 show velocities from the three most southern, western, and eastern epicenters, respectively. These simulations exhibit a small artifact, elliptical in shape, that indicates the suture of my new velocity model with that of Stephenson [2007]. In order to avoid a large discontinuity at the suture zone between the two models, I averaged points near the boundary. However, if I completely erase the contrast across this boundary, details in the models are also erased. So, I balanced the need to avoid a discontinuity that does not exist in the Earth with my desire not to erase features in the velocity models. The remaining discontinuity is visible in these images however they do not interfere with any of my interpretations. In contrast, the velocity contrast across the Seattle fault is 10% and it has a substantial effect on wave propagation. The velocity contrast across the suture zone is a few percent at most.

Waves from the northern crustal epicenters generate strong shaking throughout the northeastern part of the Seattle basin with lessor amounts of shaking to the south and southwest. There is no indication of a sharp velocity discontinuity at the basin's northern boundary. So, I interpret this focusing as a lens effect of the basin where the incident waves are focused into a narrow region. Waves from the southern crustal epicenters do not show such a broad focusing effect. Instead, the Seattle fault itself acts as a wave-guide, focusing the wave field into a band beneath downtown Seattle. This band of focused energy is further north than what I observe in Benioff zone simulations. A consistent result of the simulations is that the shallower the event, the further smeared any focusing effect is from its surface expression. This is consistent with the geometry of the incoming wave field.

Waves from the eastern crustal epicenters generate strong shaking throughout the eastern part of the Seattle basin and along the Seattle fault zone. This pattern of amplification is reminiscent of the amplification generated by the northern stations though it is more widespread from the eastern epicenters. Most of the focusing is generated from the northeast with lessor amounts from the east and southeast. In contrast the epicenters to the west show less amplification which is generated mainly from the wave guide effect of the Seattle fault for waves arriving from the west and southwest.

Benioff Zone amplifications are shown in Figures B7, B8, and B9. Figure B7 shows the average peak horizontal amplitudes for the epicenters in the left column in Figure B2. Figures B8 and B9 show the velocities generated by the middle column of epicenters and the epicenter to the far right, respectively. The shallowest events in the far west show stronger amplification along the Seattle fault zone than the intermediate depth events beneath Puget Sound. The strongest amplification comes from the event just beneath Seattle where amplifications are strong along the Seattle fault zone as well as regions north and south. It appears that shallow structure is strongly affecting the shallowest events and there is a strong focusing effect of the basin for vertically propagating waves from deep events. Events at intermediate depths and distances have the weakest amount of amplification.

The two most robust observations from these simulations are that there is strong amplification in broad areas of the Seattle Basin from waves approaching from the northeast, and that the bend in the Seattle fault just to the west of Seattle produces some strong amplification of waves approaching from the west, southwest, and south. As noted by Frankel et al., [1996], there is evidence from the 2001 Nisqually 6.8 event that waves coming from the south and west show strong amplification along the Seattle fault zone. In addition, these results are consistent with the observations of Stephenson et al., [2006] where chimneys in a limited area in the northern part of West Seattle collapsed due to unusually strong shaking during the Nisqually event.

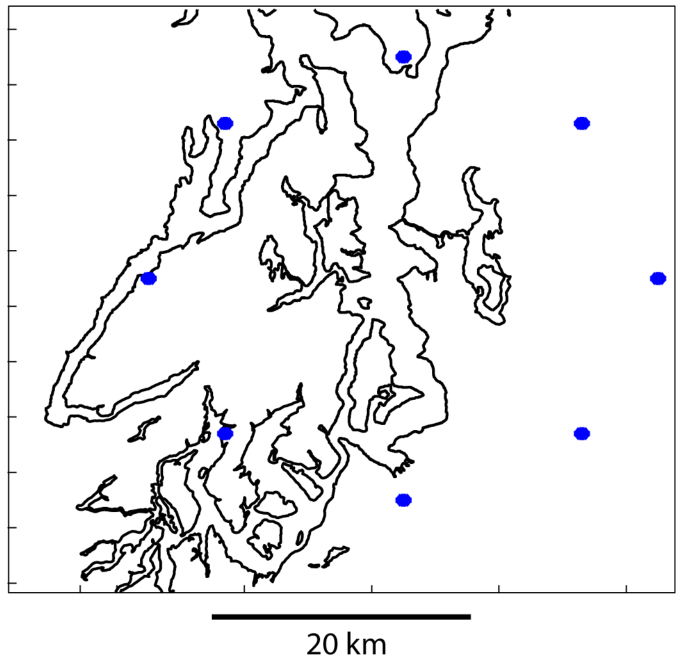

Figure B 1. Crustal Epicenters

Epicenters for crustal event simulations are shown. The depth is 10 km for all epicenters.

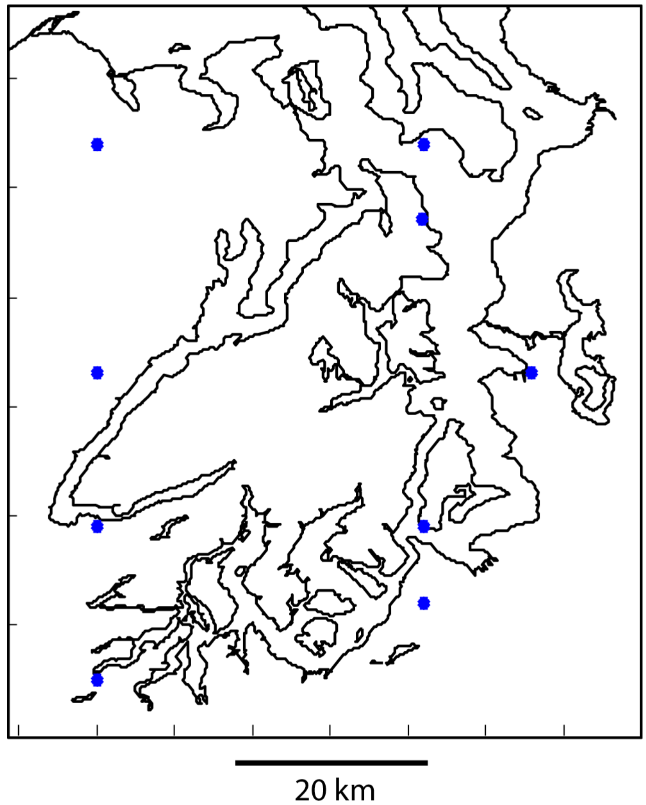

Figure B 2. Benioff Zone Epicenters

The depths are 43 km for the left column of stations, 51 km for the middle column of stations, and 54 km for the station to the far right.

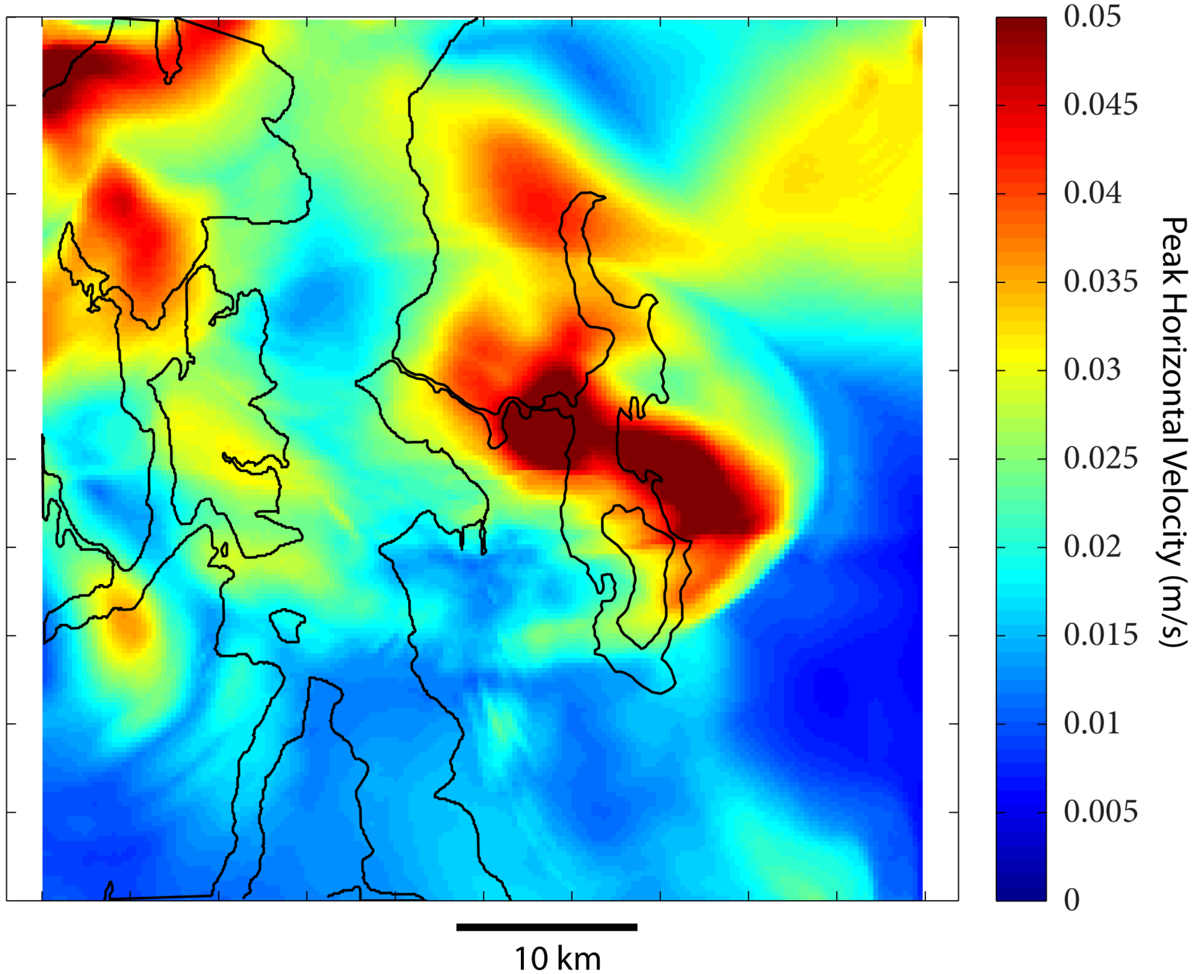

Figure B 3. North Crustal Epicenters

Peak horizontal velocity averaged from the three most northern epicenters from Figure B1.

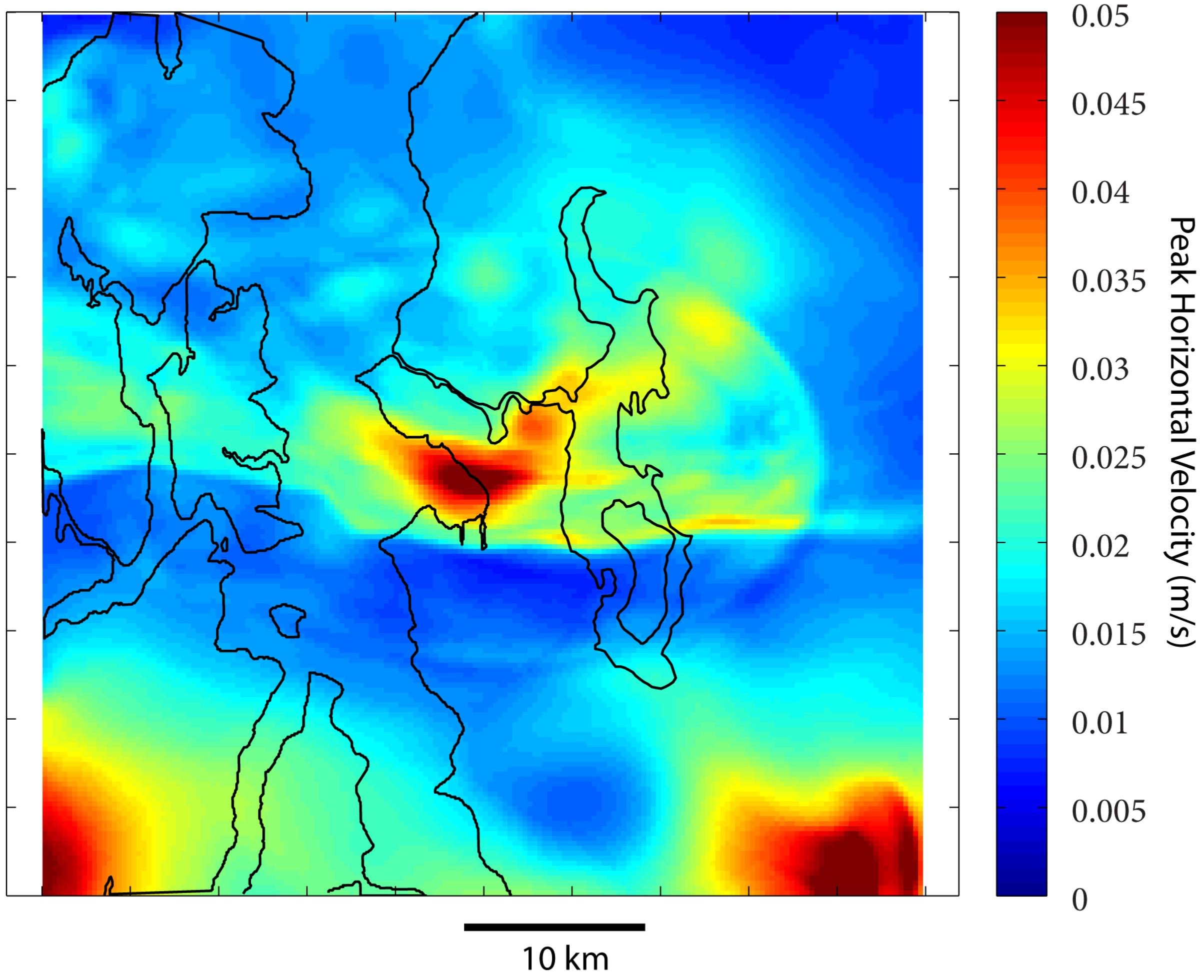

Figure B 4. South Crustal Epicenters

Peak horizontal velocity averaged from the three most southern epicenters from Figure B1.

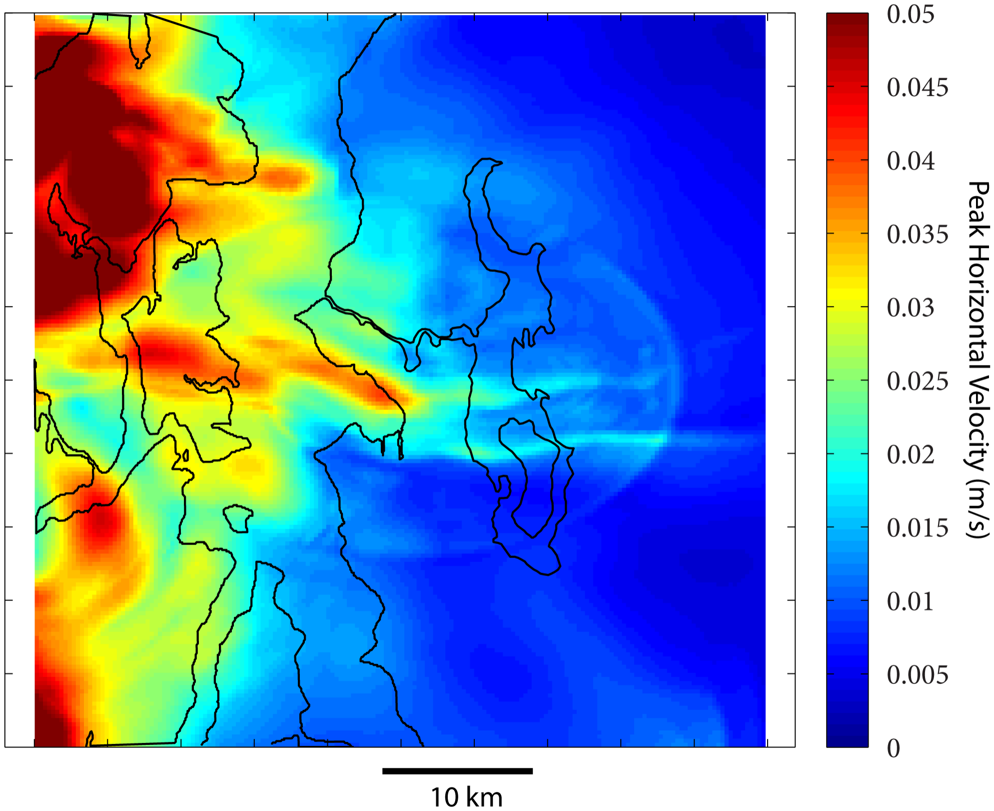

Figure B 5. West Crustal Epicenters

Peak horizontal velocity averaged from the three most western epicenters from Figure B1.

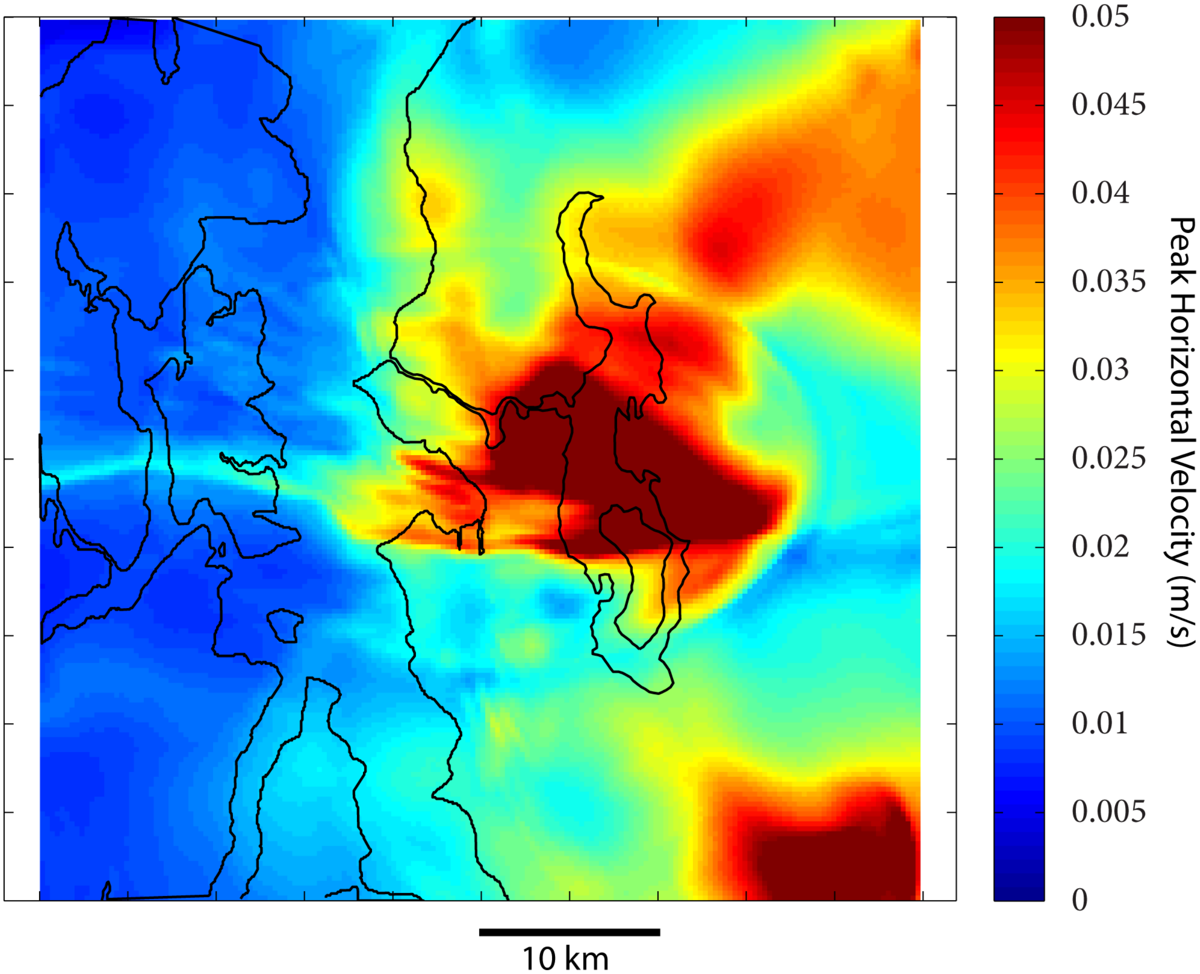

Figure B 6. East Crustal Epicenters

Peak horizontal velocity averaged from the three most eastern epicenters from Figure B1.

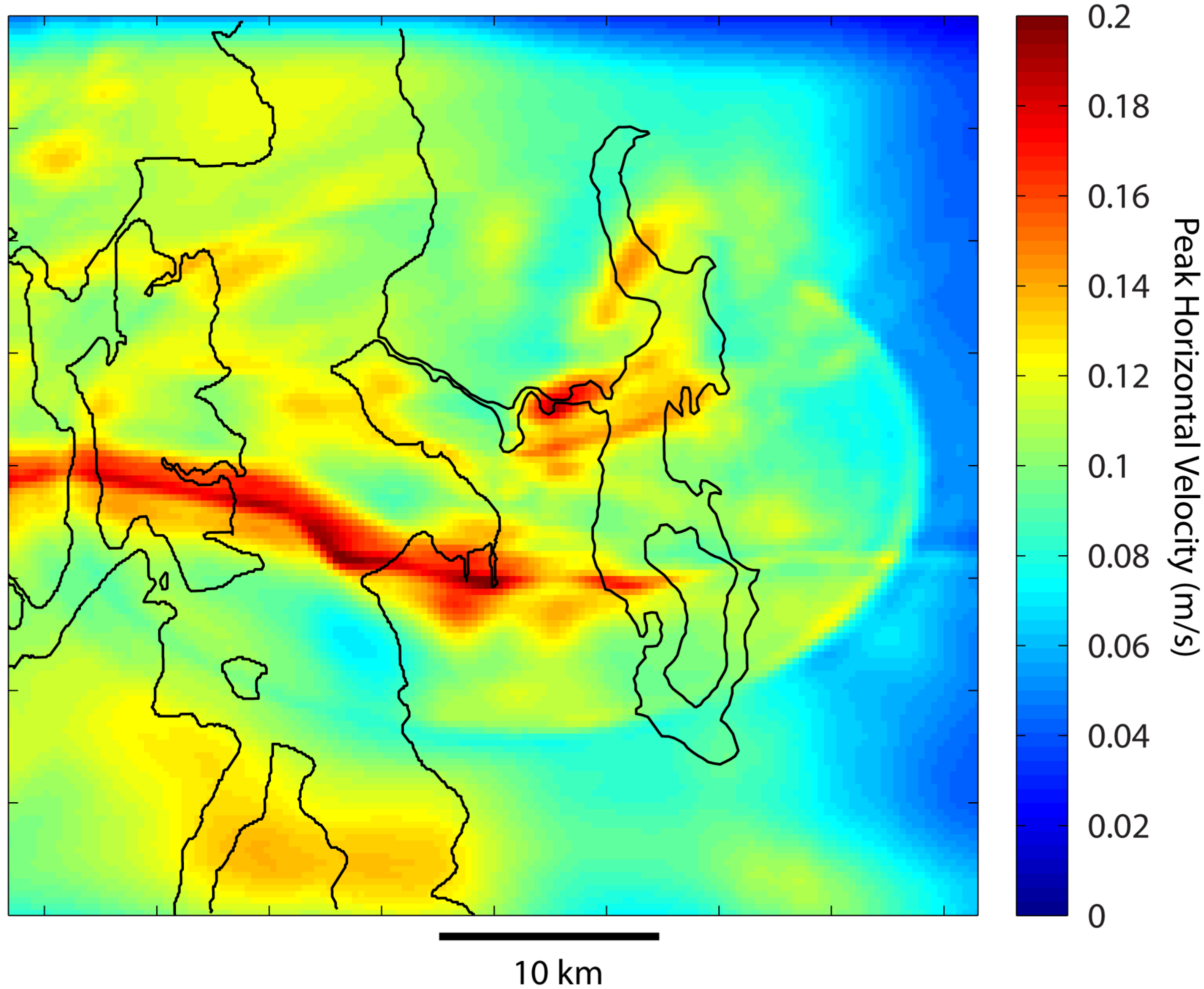

Figure B 7. West Benioff Epicenters

Peak horizontal ground velocity averaged from the four stations in the left-most column in Figure B2.

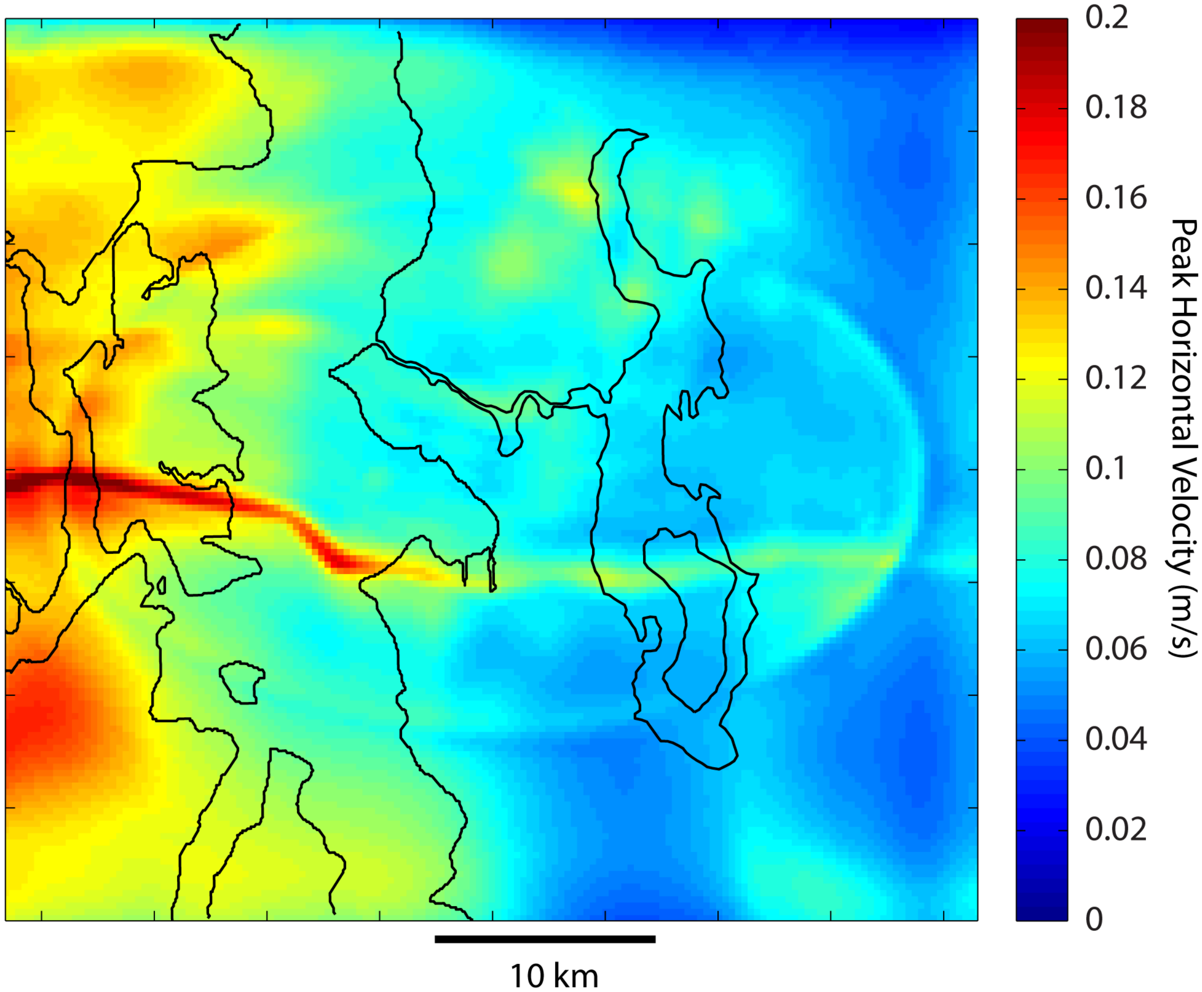

Figure B 8. Central Benioff Epicenters

Peak horizontal ground velocity averaged from the four stations in the middle column in Figure B2.

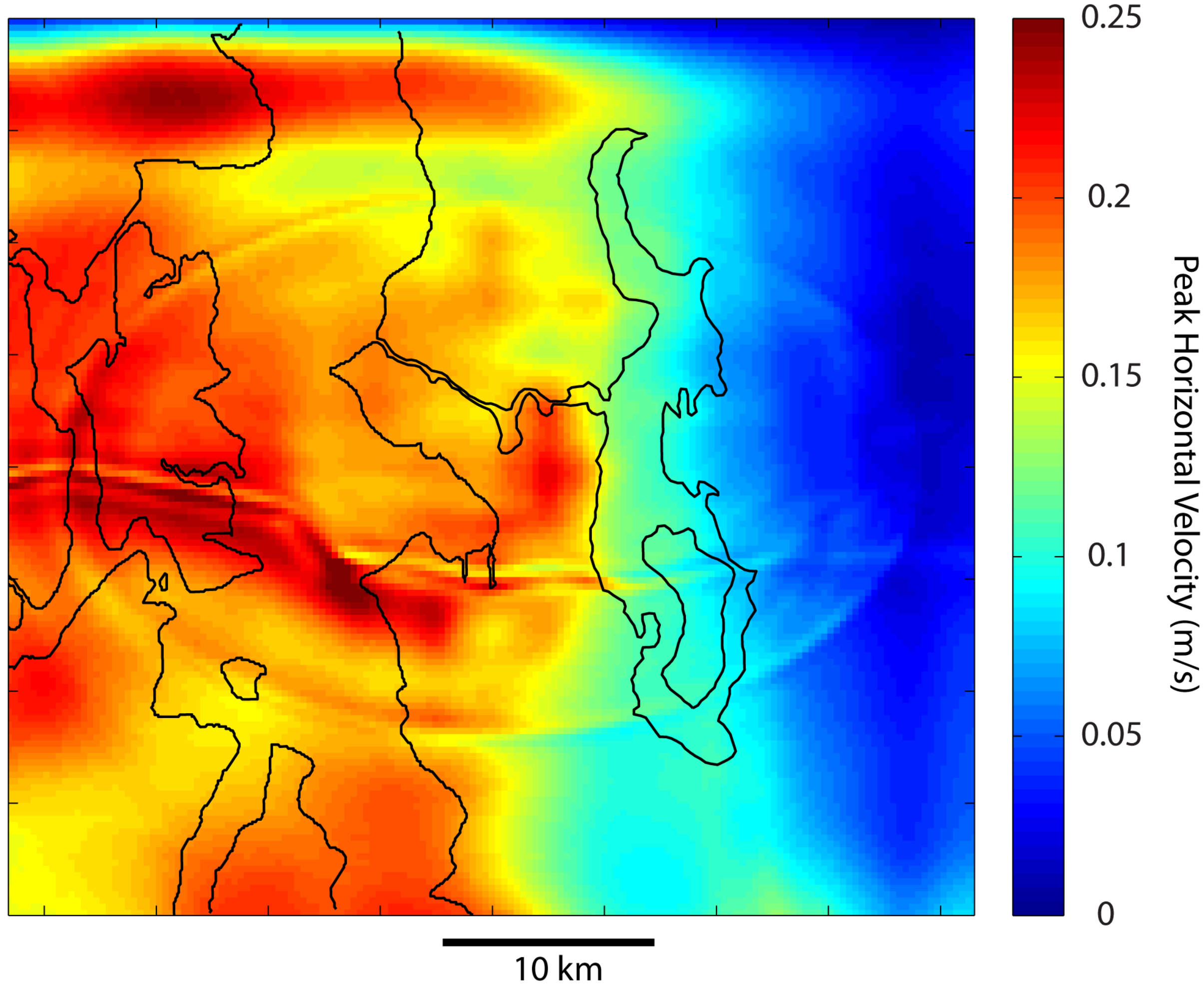

Figure B 9. East Benioff Epicenter

Peak horizontal ground velocity from the station in the far right from in Figure B2.

Alaskan Way Viaduct

The Alaskan Way Viaduct is a double-decker elevated highway along the waterfront in Seattle, Washington, which was completed in 1953. Much of it sits upon artificial fill, which covers some old mud flats at the mouth of the Duwamish River. The viaduct and the seawall on which it sits were damaged in the 6.8 Nisqually (2001) earthquake. According to the Washington State Department of Transportation (WSDOT), sections of the viaduct have settled 12-16 cm, with a similar amount of horizontal movement in the 9 years following this event. Efforts to halt the settling have been successful, however it is not known whether or not the structure could withstand another such event without partial collapse. In 2012 or soon thereafter, the viaduct is scheduled for demolition and the seawall is scheduled for major reconstruction.

According to a series of reports commissioned by the WSDOT [*Eberhard et al.*, 1995; *Knaebel et al.*, 1995; *Kramer et al.*, 1995] and summarized by Kramer and Eberhard [1995], the viaduct and seawall may not withstand design-level motions, defined as 10 percent chance of exceedance in 50 years. In the WSDOT reports, design-level motions are described as about three times higher than the peak acceleration produced by the 6.5 Seattle-Tacoma (1965) earthquake, which was 60%g at 3.3 Hz in the vicinity [*Ichinose et al.*, 2004]. According to a more recent study, design-level motions at this recurrence rate should be 80-145%g spectral acceleration at 1 Hz [*Frankel et al.*, 2007]. Among the conclusions of the WSDOT reports are: the design level ground motion represents considerably stronger earthquake shaking than the viaduct has been subjected to in the past, design-level motion would likely cause heavy damage or collapse, and liquefaction is expected to occur in a design-level ground motion and could cause multiple sections of the viaduct to collapse.

According to Kramer and Eberhard [1995], the manner in which the waterfront fill beneath the Alaskan Way Viaduct was placed is a virtual recipe for creating a liquefiable soil deposit. If the seawall were to fail during an earthquake, it would likely take sections of the viaduct with it into Elliot Bay. It is important to note that these reports were written prior to the 6.8 Nisqually (2001) earthquake. Though the viaduct did sustain some damage during this earthquake, no part of the structure collapsed and the highway was reopened after inspection and repairs.

With only 6 channels and two sensor locations, I cannot comprehensively analyze the response of the viaduct as a whole to ambient and earthquake forcing. However, I can monitor how the structure's response at the instrumented location changes over time to different inputs. Since I know that this structure is deficient and is located in a high-risk area, the data I collect may be useful for comparison to structures with modern designs. The stiffness of a structure can be monitored by observing its resonant frequencies. Since the frequencies of free oscillations are proportional to the square root of the stiffness, I can use the resonant frequencies as a proxy for stiffness. If the stiffness of a structure is reduced either gradually or suddenly, then it may indicate damage or the weakening of the structure or soils around the foundation [*Michel and Gueguen*, 2010]. Factors that have been observed to affect the resonant frequencies of structures elsewhere include temperature, precipitation, soil water content, wind, structural modifications, changes in mass, damage, and changes in forcing [*Clinton et al.*, 2006]. In order to use variations in resonant frequency to identify damage to a structure, these other factors must be understood.

Since September 2008, the United States Geological Survey (USGS) has provided a 6-channel K2 Episensor strong-motion instrument, recording at 100 samples per second, to monitor the structure in the region where the viaduct has had the greatest amount of settling after the Nisqually earthquake. Three channels record at the top of a column and three channels record on the sidewalk at the base of the same column. I recorded continuously for a full week just after installation, and then set the instrument to record 15-minute continuous intervals every hour, which was later reduced to every two hours. In addition, the instrument was set to trigger for earthquakes, which resulted in triggering on many transient motions caused by vehicles as well as earthquakes. I had to set the triggering threshold high to avoid a trigger every time a vehicle passes, which resulted in not triggering on many small earthquakes less than about magnitude 3.5.

The horizontal components were aligned with the structure, rather than compass points. I use the term "transverse" to indicate the component that measures motions perpendicular to traffic and "inline" to indicate the component that measure motions parallel with traffic. The inline component is oriented approximately 30 degrees west of north and the transverse component is oriented 90 degrees clockwise from the inline component.
I calculated the amplitude spectrum for all six components over two-hour intervals to coincide with the timing of my sampling windows. In addition to examining the amplitude spectrum over the entire duration of the recording, I calculated averages for each day of the week as well as by grouping days into weekdays and weekends. To help in identifying fundamental modes of the structure, I looked at upper and lower traces simultaneously to verify that the phase and amplitude relationships were consistent with what was expected for the fundamental mode.

For comparison and analysis, I calculated the amplitude of the signal and obtained temperature, wind, and precipitation data collected at the University of Washington using the same intervals and averaging procedures that I used for the amplitude spectrum. Since both sensors were strongly affected by the motions of the viaduct, I also collected data from a nearby USGS urban strong motion station, PIO2, for use as a free-field site for my analysis of the 4.5 Kingston (2009) earthquake. This station is located a few hundred meters to the east of the viaduct. By comparing data collected at the viaduct with this free-field station, I was able to estimate the amount of amplification at the viaduct over the input ground motion.

Analysis and Results

According to the WSDOT reports [*Eberhard et al.*, 1995; *Knaebel et al.*, 1995], the two most important modes of a single section of the viaduct are inline and transverse bending. Most sections of the structure consist of four pairs of columns and three spans. An expansion joint connects the roadways of adjacent sections. My instruments were on an interior column of a straight section. Complicating details include on-ramps and off-ramps; there is an on-ramp merging into the lower level of the instrumented section. In addition, the roadway begins to curve in the section just to the south of the one that was instrumented. As such, it is possible that there could be a transfer of energy between the two principal horizontal bending modes and I do not expect that the sections respond entirely independently from one another.

In the WSDOT reports [*Eberhard et al.*, 1995; *Knaebel et al.*, 1995], the authors calculate theoretical fundamental frequencies of 1.13 Hz for inline bending and 1.32 Hz for transverse bending for a typical section of roadway. These values were determined by modeling a section of roadway independent of adjacent sections. In my data there are two peaks on both horizontal components at 1.85 Hz and 2.15 Hz, though they are both much stronger and sharper on the transverse component (Figure C1). These modes appear fundamental because motions on the upper deck and at ground level are in phase. At higher frequencies, there is also apparent contamination between modes on the two horizontal components. At 6.5, 7.0, and 9.1 Hz there are strong peaks on the inline component with some apparent contamination on the transverse component and at 7.8 Hz there is a strong peak on the transverse component with some apparent contamination on the inline component.

In addition to horizontal motion, I also analyzed vertical dilatation and compression even though this mode of deformation is not a major concern for seismic hazards. I observe the fundamental frequency at 5.3 Hz and two more peaks between 6-7 Hz that may be related to similar peaks on the inline component. There is a smaller difference between the amplitudes recorded at the upper and lower components in the vertical direction than between the upper and lower components in the horizontal directions, which is consistent with my expectations based on the relative stiffness of the modes they represent.

I looked at daily, weekly, and long-term frequency variations in the lowest frequency peak of the transverse and vertical components as well as a few of the higher frequency peaks. There is no apparent seasonal or long-term trend over the course of the recording period. Correlations with temperature, precipitation, or wind speed were poor. There is a strong anti-correlation between the level of shaking due to traffic and the fundamental frequencies on the transverse components (Figure C2). Frequency reduction is about 1% for a five-fold increase in shaking amplitude. Peak accelerations rarely exceed 3-4%g due to passing vehicle traffic under ambient conditions. This anti-correlation can also be seen on the vertical component. In addition to shaking due to daily rush-hour traffic, this relationship also holds on weekends when traffic patterns are different and generally lighter (Figure C4), during a winter storm in December 2008 when traffic was very light, and on days in which the viaduct was closed to traffic during inspections. In all of these cases, the fundamental frequencies increase during periods of low traffic, and decrease during periods of high traffic. Traffic-induced shaking can be applied at the upper deck, lower deck, and from vehicles passing beneath the structure. Passing vehicles excite a variety of frequencies that apparently depend on vehicle mass, speed, and location. Most "seismic" energy that I record is generated when vehicles pass over the expansion joints on the roadway. I cannot identify the method of excitation by passing vehicles based on the frequency content, but observe consistent spectral energy spikes ranging all the way from the fundamental frequency up to about 40 Hz, just shy of the Nyquist frequency of 50 Hz. Higher energy pulses tend to have a more broadband signal while the lowest energy pulses are confined to frequencies between 15-25 Hz.

The recordings of the 4.5 Kingston (2009) earthquake give us insight on what might happen during a bigger event (Figure C5). The maximum acceleration that I recorded on the top deck of the viaduct during this event was 4%g. This is comparable to the acceleration generated by passing vehicles, which can be identified on the time series during periods of high amplitude that appear in the viaduct recordings, but not at station PIO2. Examples of signals generated by traffic are located near 45 seconds and between 80 and 100 seconds of the earthquake recordings. Oscillations on the viaduct that are generated by the earthquake are nearly monotonic, while the oscillations generated by passing vehicles are more broadband and contain higher frequencies. The peak acceleration at the top of the viaduct was ~4x stronger than at the base and ~7x stronger than at the free-field site during the earthquake. The peak acceleration at the base of the viaduct was about ~1.7x stronger than at the free-field site; the base site was no doubt effected by the viaduct itself. The most obvious feature of the earthquake recording is that nearly all of the energy was concentrated at a single frequency ~1.7 Hz (Figure C5), and that the shaking lasted for around 50 seconds at this frequency, much longer than what would be expected for an earthquake of this size and distance. The long duration may be due in part to the effect of the Seattle basin; sedimentary basins are known to affect the amplitude and duration of shaking during earthquakes [*Graves et al.*, 1998; *Stephenson et al.*, 2006]. In contrast, during ambient conditions, energy is distributed over many different frequencies (Figures 1 and 5). It appears that inline and transverse bending are highly coupled, especially during earthquakes.

Conclusions

My two most important observations were the daily variations in the frequencies of the free oscillations and the viaduct's response during the 4.5 Kingston (2009) earthquake. To explain the daily variations in frequencies, I considered temperature, wind, water table fluctuations caused by ocean tides (ground level at the viaduct is only a few meters above sea level and a few tens of meters from the waterfront), the mass of the vehicles, and shaking caused by vehicles. Since the anti-correlation follows so closely with the level of shaking due to traffic, and the correlation is poor with temperature, wind, or tides, I ruled these other factors out as important. The mass of the vehicles is small compared to the mass of the structure and not enough to reduce the frequencies of the free oscillations by the observed amount, though they still theoretically have some small effect.

If the amplitude of shaking caused by vehicle traffic is the cause of the reduction in frequency, there are at least two possible explanations. First, the viaduct could be acting like a damped oscillator. In this explanation, the frequency of the free oscillations is reduced when the amplitude of the oscillations increases, due to damping. The second explanation is that the soils around the foundation of the structure are disturbed during periods of stronger shaking, slightly reducing their stiffness. When the level of shaking is reduced, the soils "heal" and return to their original stiffness. Any lag between the onset of a change in the amplitude of shaking and a change in the resonant frequency is too short to resolve, less than two hours. If such a lag exists, it would support the explanation that the viaduct/soil system softens slightly due to higher amplitude shaking, and "heals" when shaking is reduced. There would be no lag for the damped oscillator explanation. Though I believe that the main cause of the apparent reduction in stiffness is due to softening of the foundation/soil system, damping is also a likely contributor.

According to the Pacific Northwest Seismic Network (PNSN), peak ground accelerations recorded during the 6.8 Nisqually (2001) earthquake were 5-30%g in the vicinity of the viaduct. If the amplification factors that I observed scale linearly, then that means the shaking was 8-50%g at the base of the viaduct and 35-200% on the top deck. It is unlikely that accelerations scale linearly or were as high as this upper bound because the structure would not likely still be standing. Recording a few more non-destructive moderate or larger events of different sizes would help to establish a scaling relationship; my monitoring is ongoing. For structures with a longer life expectancy, a scaling relationship could be established by analyzing the structure's response to a variety of non-destructive events.

Unlike buildings, elevated roadways are regularly subjected to shaking, generated by passing vehicles, that are equivalent in magnitude to that of small to moderate earthquakes, though with different forcing frequencies and durations. I find no evidence for measurable, instantaneous changes in the stiffness or resonant frequencies of the structure during these impulsive events, despite the evidence for a cumulative effect of heavy, daytime traffic. Since the points of application and direction of these forces are more numerous, many unidentified modes of oscillation are excited, unlike earthquakes where the force is only applied at the base and most of the energy is associated with a single harmonic mode (Figure C5).

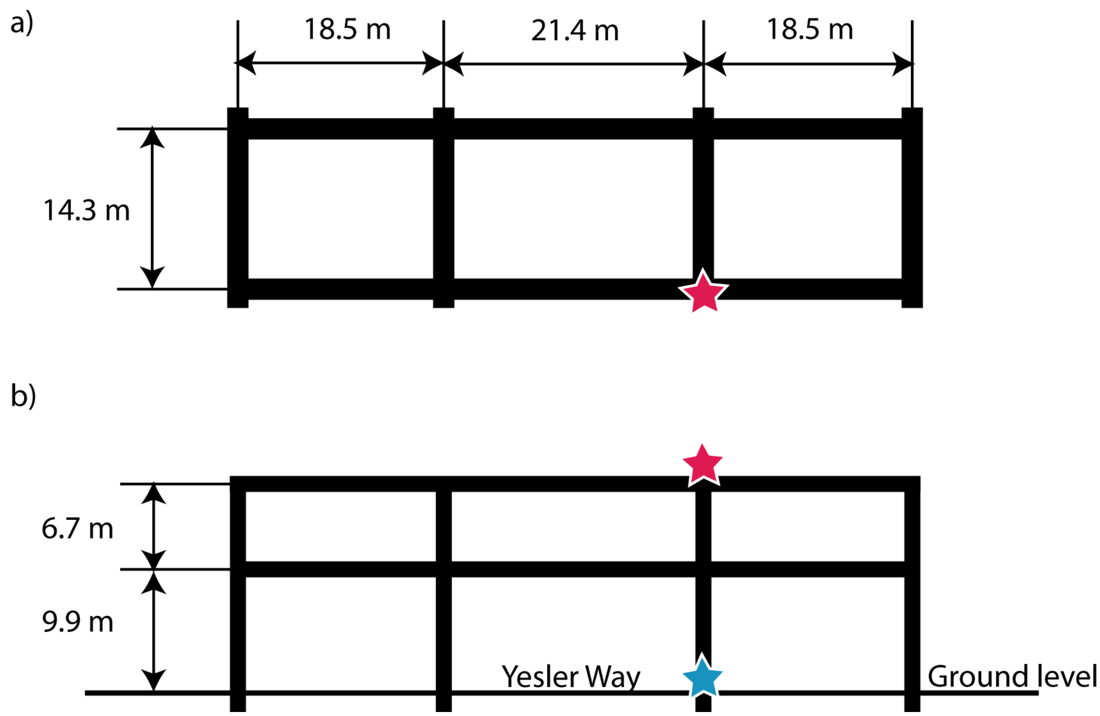

Figure C 1. Schematic Drawing

Schematic drawing of a segment of the Alaskan Way Viaduct showing a) top view and b) side view. The the red star indicates the location of the upper sensor. The blue star indicates the location of the lower sensor.

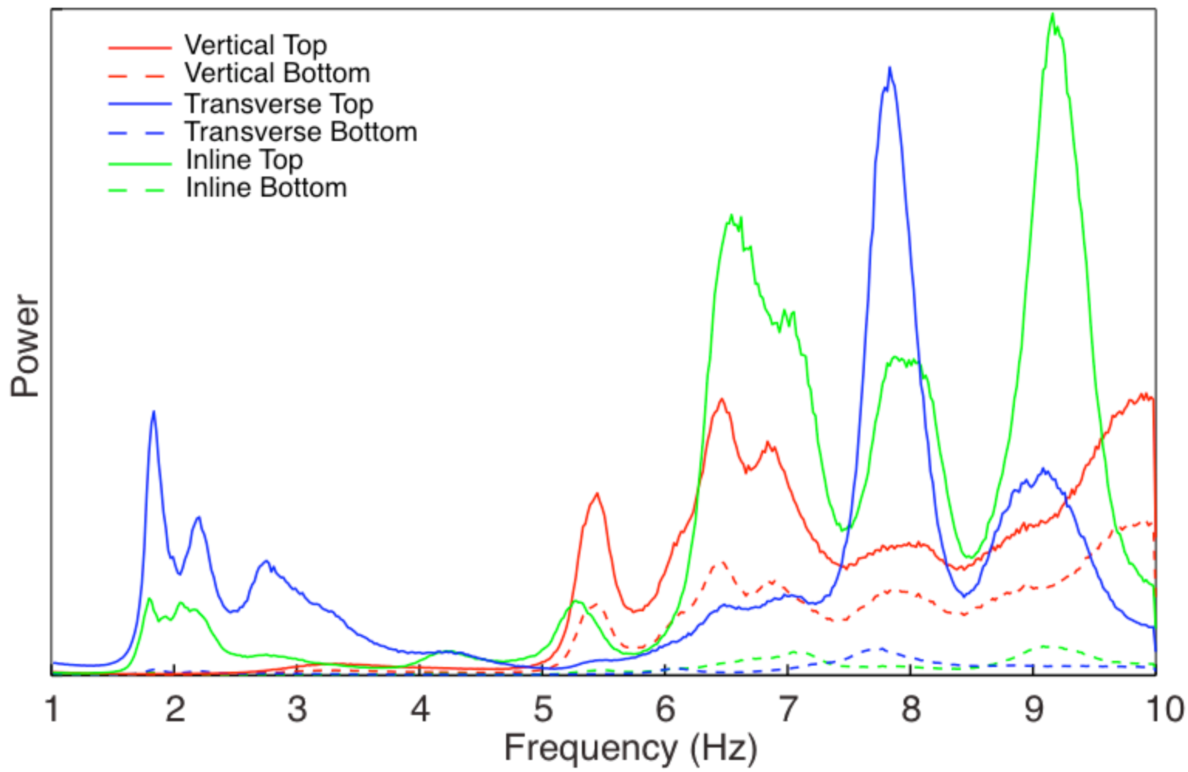

Figure C 2. Amplitude Spectrum

Shown are the average amplitude spectra for the (a) vertical components, (b) transverse components, and (c) inline components.

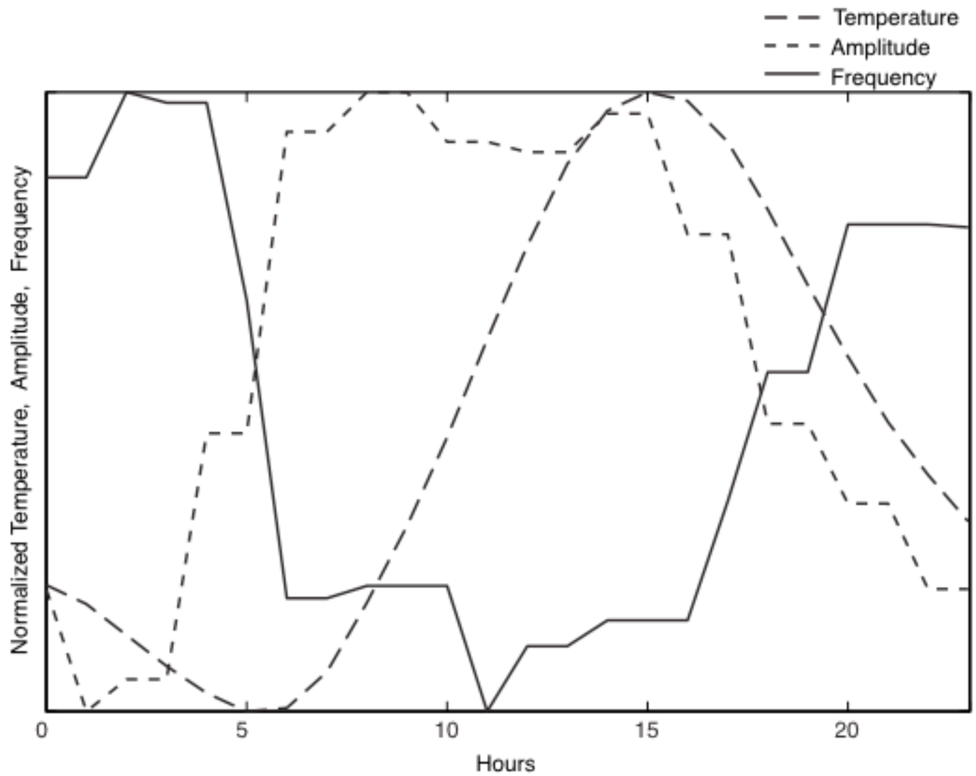

Figure C 3. Temperature, Amplitude, Frequency

Shown are normalized average daily values (Monday-Friday) for the transverse component on the upper sensor. The frequency curve represents the drifting of the fundamental frequency over the course of one day. The amplitude of the shaking is highest during the day with two peaks corresponding to morning and evening rush hour. The frequency is lowest when the amplitude is highest. There is no apparent relationship between the temperature and frequency.

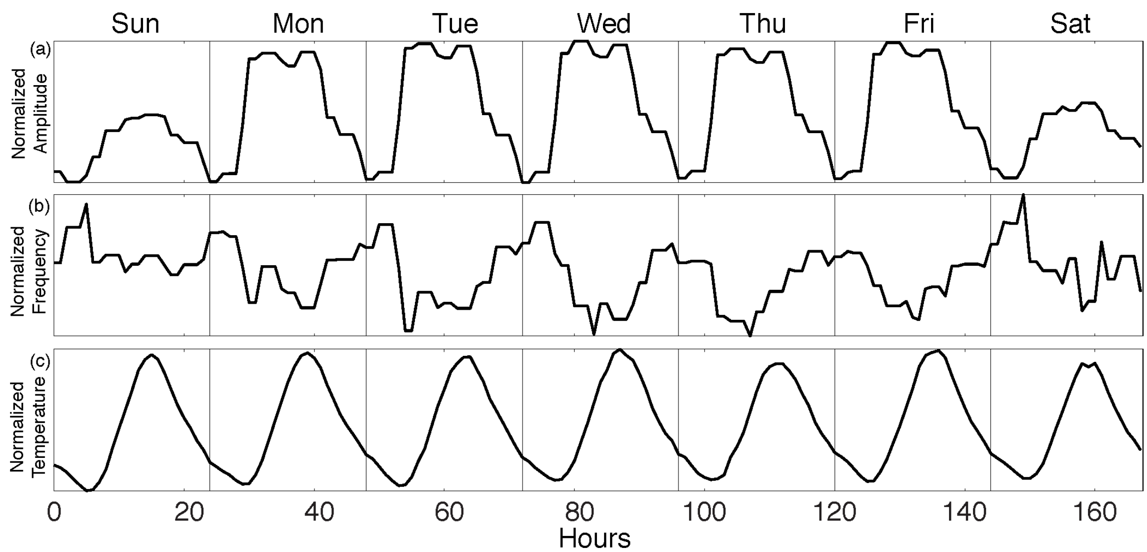

Figure C 4. Weekly Amplitude, Frequency, and Temperature

Shown are normalized average weekly values for the transverse component of the upper sensor for (a) amplitude, (b) frequency, and (c) temperature. Amplitudes are noticeably lower and frequencies are noticeably higher on the weekend compared to the corresponding time of day during the week. There is no apparent relationship between temperature and frequency. The average annual temperature range over 24 hours is 5.3 °C. The minimum frequency on this figure is 1.83 Hz and the maximum is 1.87 Hz, which represents a 2.2% difference. The average amplitude is never zero since there is always some ambient noise and the peak average amplitude is 5.4 times the minimum value.

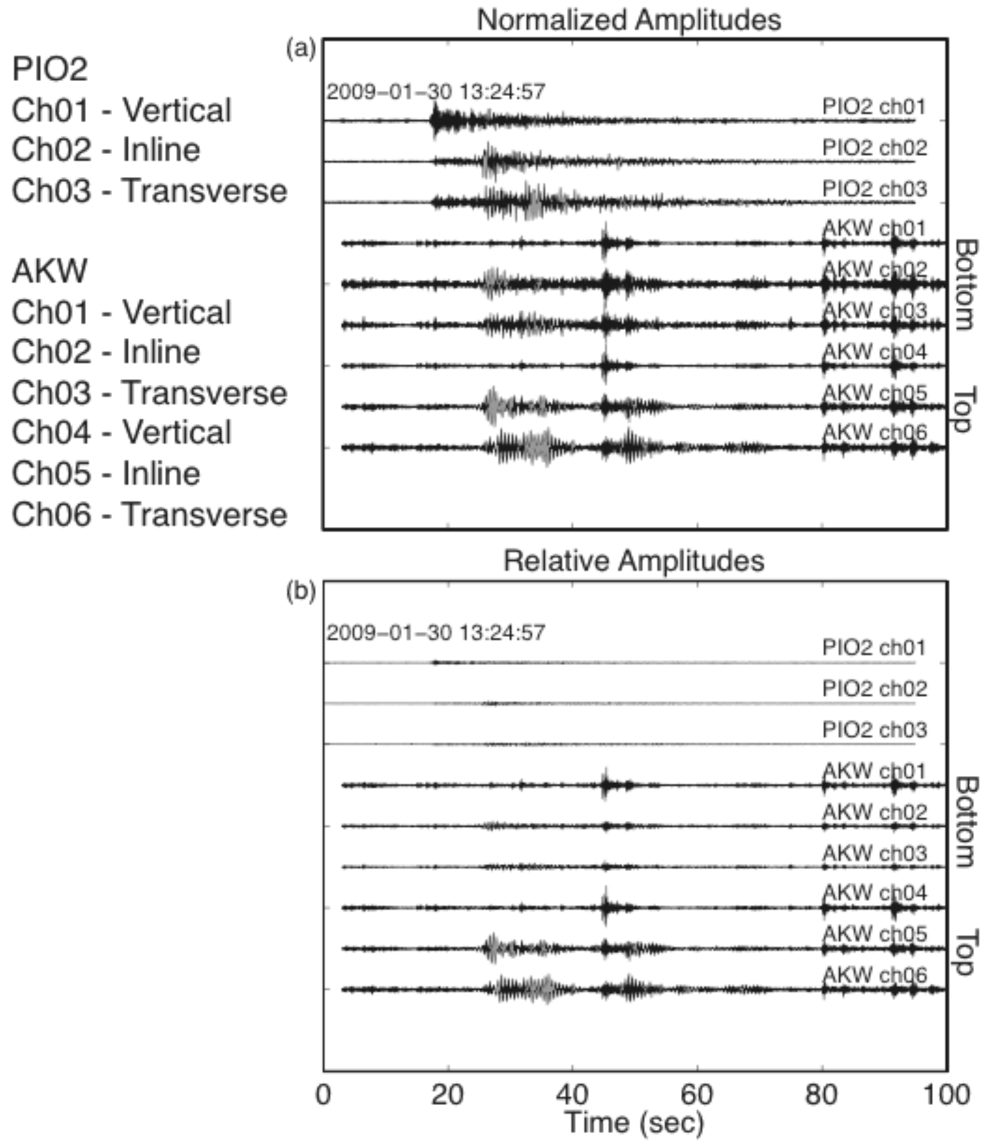

Figure C 5. Kingston Event

Shown are acceleration seismograms for the 4.5 Kingston (2009) earthquake, (a) normalized amplitudes, (b) relative amplitudes. Vehicles traveling on the viaduct generate the high frequency signals that appear on AKW components, but not on PIO2 components. AKW channels 1-3 are located at ground level and AKW channels 4-6 are located on the top deck of the viaduct. Station PIO2 is located a few hundreds of meters away from the viaduct.

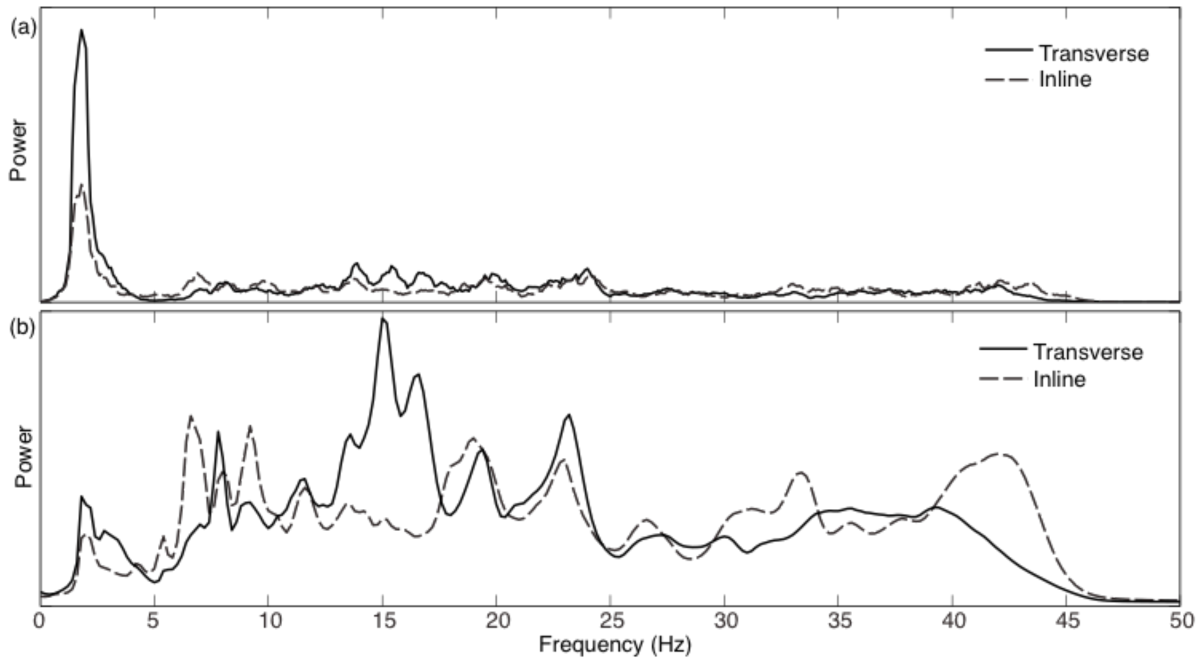

Figure C 6. Earthquake and Ambient

Shown (a) are the power spectrum during the 4.5 Kingston (2009) earthquake and (b) the power spectrum during ambient conditions.

Non-linear Response in Broadband Instruments

I observe that broadband seismometers may produce artifact long period signals that resemble impulse responses, similar to a step in acceleration, in the presence of shaking as moderate as 0.2%g. This observation accords with recent observations in Europe and elsewhere with similar instruments e.g., [*Zahradnik and Plesinger*, 2005]. I present two case studies. For both the October 8, 2006 M4.5 earthquake near Mt. Rainier in the Pacific Northwest and an M5.0 event on 9/29/2004 in Southern California, artifact signals, possible step tilts, and apparent sensor problems are observed as far as about 200 km from the epicenters. Such long-period artifacts, if not recognized, complicate and degrade estimation of source parameters of moderate and larger earthquakes on regional networks. The exact cause of the artifacts currently remains obscure, but may require alterations to instrument installation and/or design strategies [*Delorey et al.*, 2008].

Introduction

Regional seismic networks (RSNs) monitor local seismic activity, provide information for hazard assessment, and support basic research. RSNs provide hypocenter locations, determine source parameters for small and medium sized earthquakes, estimate local velocity structure, and estimate ground motion levels from larger earthquakes. While contributing to several RSN data products, the primary role of broadband sensors in RSN operations is often to provide critical data used to determine earthquake source characteristics accurately and quickly. This information is contained particularly in the longer period signals. This environment of operation differs from that found in global network operations, chiefly because at teleseismic distances ground motions are usually extremely small, and high frequencies have been stripped from the signal by attenuation over long paths. At regional distances, in contrast, peak ground motions can be moderate to strong at stations within a few hundred kilometers of small to medium sized earthquakes, and the spectrum of ground motion may be rich in high frequencies. It is, nevertheless, necessary for broadband instruments to behave linearly under these conditions. In the wake of Earthscope's Transportable Array, many regional networks in the US are being augmented by broadband instruments and it is within that context that I consider the suitability of these instruments to the needs of regional networks; in this case the Pacific Northwest Seismic Network.

I first noted apparent signal irregularities within regional records of a moderate regional earthquake. In the process of investigating the cause of apparent artifact signals, suspecting limitations in the recording system, I discovered documentation of similar problems in another paper [*Zahradnik and Plesinger*, 2005]. Then I verified that similar problems are present in a third regional network with similar instrumentation (the California Integrated Seismic Network, CISN), then explored why these problems arise.

The observed artifact signals are similar to the expected response to a step in acceleration. If the baseline deviations I observe are solely the product of a transient elastic seismic wave at the instrument, then it would represent a non-linear response. Alternatively, the sensors may be experiencing motion that is not simply caused by an elastic wave; the sensor may be producing the correct response to a quasi-static tilt. I examine these two possibilities: that the instrument is producing a non-linear response to an elastic wave or that the instrument is recording a ground motion that is not linear and elastic, as would be the case for permanent deformation.

Discussion

I collect the three-component broadband data from instruments within 150 km of the October 8, 2006 M4.5 event near Mt. Rainier from the EarthScope CAFE experiment and the EarthScope Transportable Array. The Transportable Array uses a mix of Guralp CMG3T and Streckeisen STS-2 instruments recording at 40 samples per second and the CAFE experiment uses Guralp CMG3T instruments recording at 50 samples per second (Creager, 2007, pers. comm.) and [*Simpson*, 2006] (Figure D1). For each trace I remove the mean, remove the trend, deconvolve the instrument response, convert to displacement, and apply a lowpass filter with a corner frequency of 0.1 Hz. Then, all traces are manually inspected for the presence of "suspect" transient signals. In some cases I use alternative signal processing techniques to highlight suspect signals, including inspecting acceleration and velocity in addition to displacement, or modifying the corner frequency on the lowpass filter. A typical non-linear waveform is distinguished by a step in the acceleration followed by a recovery with a period of a hundred seconds or more (Figure D2). From the point of view of RSN operations, the long period transient is noise that could lead to the incorrect analysis of an earthquake's source characteristics unless either corrected or recognized and the recording eliminated from further analysis. However, this type of noise is not stationary, but rather signal-generated, and so I proceeded to try to recognize under what conditions it is introduced into the data.

My analysis indicates that artifact transients contaminated data from at least 32 stations of the 75 I examined. This number is a lower bound because at some stations high levels of ambient noise may have obscured long-period transients. The relative displacement amplitudes of horizontal artifacts processed as described above are shown in Figure D3.

Figure D4 reveals the polarizations of horizontal excursions. Stations closer to the earthquake (e.g., such as S090, S100) tend to have larger excursions but there are several exceptions. I can identify no strong patterns in the direction of polarization of the horizontal excursions, but note a weak tendency for them to point away from the earthquake epicenter and a stronger tendency for non-linear behavior on the north component than the east component. Some stations show excursions on the vertical component and most of these are close (<75 km) to the earthquake epicenter. The time of the non-linear excursions corresponds roughly with the strongest shaking, which is during the arrival of the S-wave. In Figures D5 and D6, I examine the relationship between artifact transients and spectral acceleration. There appears to be no precise threshold for non-linearity, but stations tend to go non-linear for spectral accelerations between 10-6 and 10-7 m/s2. I note that this representation of the accelerations is limited to the passband below the Nyquist frequency of the sampled data (either 20 or 25 Hz). The sensor, and its active feedback circuitry, may be exposed to, and respond to, frequencies higher than this passband, if present in the seismic wave field.

I observe similar artifacts on at least 22 broadband stations in southern California due to an M5.0 event on 9/29/2004 (Figures D7 and D8). The distance between the event and the most distant station identified as exhibiting non-linear behavior is 249 km, farther than that observed for the Rainier event, and consistent with the greater magnitude of the California event. Peak ground acceleration is 2.2%g for the closest station and some of the stations show evidence of clipping. Like the Rainier event, there is no clear pattern to the polarization of the horizontal excursions and stations close to the event are more likely to show non-linear behavior than more distant stations.

Causes

I investigate the causes of non-linear behavior in broadband instruments during moderate shaking. At least two of the closest instruments, S090, N120, have clipped in the digitizer and probably in the seismometer as well during peak accelerations of 1%g and 0.25%g, respectively. However, clipping, which occurs at ~1 cm/s for the Guralp CMG3T and 1.3 cm/s for the Streckeisen STS-2, is not a widespread problem for this event. Measured peak velocities for the two clipped stations are 1.7 cm/s for S090 and 0.86 cm for N120.
In the absence of clipping, the most commonly supposed cause of non-linear behavior is tilting of the instrument [Zahradnik and Plesinger, 2005]. A small step in acceleration, caused by a permanent tilt, can explain the observed velocity excursions in the raw data. It should be noted that a step in acceleration on a horizontal component could be caused by both an impulsive and permanent horizontal displacement and a permanent tilt around the appropriate horizontal axis, but not by a vertical displacement. The response to a tilt could be compared to an "equivalent displacement", the horizontal displacement that would be required to produce the same signal. In general quasi-static tilts could arise from ground deformation of tectonic origin, from instabilities in instrument installation, or from local failures within the instrument pier (e.g., crack formation caused by shaking, or shifting in objects surrounding the sensor). In fortunate cases, seismograms can be separated into ground motion and tilt [*Battaglia et al.*, 2000; *Boore et al.*, 2002; *Graizer*, 2006; *Wielandt and Forbriger*, 1999; *Wiens et al.*, 2005]. I show that the non-linear signal recorded on station S100 (BHN) can be modeled as the response to a step in acceleration as would be expected for instrument tilt (Figure 9). My case differs from most of these cited in that I am using a broadband sensor

undergoing moderately strong shaking, these other cases have either strong motion sensors or tilting in the absence of strong shaking.

I perform an experiment using a Streckeisen STS-2 instrument, successively lifting each leg a controlled amount to produce controlled tilts. This produces acceleration steps and resulting "calibration pulses" in the expected ratios on north and east components with no vertical signal. It is clear from this experiment that vertical movement on one of the three feet would not cause the observed dominant north polarization suggesting that more than one of the three legs of the instrument is affected. On both the Guralp CMG3T and the Streckeisen STS-2 instruments, there is a foot at the westerly compass direction and the three feet are at ~120º distance from each other. This experiment does not explain observations of the behavior of the vertical component.

Due to the incoherence of the patterns in the apparent tilt direction, and the vastly greater amplitude than expected from the earthquake's moment release, the evidence suggest that any tilting is local, perhaps as local as within the instrument vault. In the presence of moderate shaking, there could be some settling of the instrument platform. For Transportable Array and CAFE station stations, after the instruments are installed, the vaults are filled with sand to reduce long period noise. Jostling at the peak 3-4Hz motions and small fraction of g may be sufficient to shift the sand, causing small tilts in the instrument. If events like this happened once per week, and the occurrence of such artifacts diminished over time, it would be evidence that the installations really were settling. However, this behavior is observed at southern California stations that have experienced many moderate earthquakes, including an event on the previous day to the one presented here. Some of the same stations show non-linear behavior of a similar magnitude for both events.

Some instruments show excursions that are almost exclusively on one of the horizontal components (Figure D4) with a preference for the north-south component. While it is possible that east-west excursions could be the result of an elevation change in one foot, a purely north-south excursion due to sensor foot settlement would require elevation changes in at least two feet. Additionally, it is more likely for a foot to settle than to be elevated and I observe excursions in the east-west component in both east and west directions. So, I must consider causes other than ground tilt affecting only one or two feet, to explain at least some of the excursions.

Another possible cause of the artifacts is an inherently non-linear response of the sensors to ground motion. Higher frequency signals observed at regional distances might be rectified or distorted, resulting in apparent low-frequency products. The impulsiveness of the signal might be important in generating spurious long period offsets, leading to further variation between stations and apparent ground motion levels at which the artifacts are generated. Both types of instruments have similar active feedback circuits and therefore could be susceptible to the same problems without resorting to external explanations. However, in the case of the Streckeisen STS-2 instruments, the three output components (north, east, up) are electronically generated from three cube-cornered sensors. It seems unlikely that a non-linear response of the sensors would manifest themselves on the horizontal output components, but not as frequently on the vertical output component. Also, the Guralp instruments resolve the three output components mechanically and show the same variation of behavior in the output components as the Streckeisen instruments, supporting the argument that the cause of artifacts is external to the instruments.

Impacts

The introduction of transient long-period artifacts into regional broadband ground motion data for moderate to large earthquakes is a problem of grave concern to RSNs. Analyses that depend on accurate ground motions at periods of 10s – 100s, such as waveform-matching moment tensor estimates, become fraught with uncertainty. As illustrated in Figure D9, see also [*Zahradnik and Plesinger*, 2005], if the artifact can be understood well enough to be modeled theoretically, it may be removed and its impact mitigated. At a minimum, if the conditions under which they may affect data can be adequately understood, automatic-processing systems may be able to flag data with potential artifact problems and not use it in automatic analyses. Also, many applications of seismic data filter out long-period data (>100s) and therefore will not be negatively impacted by the long-period non-linear behavior I describe. Applications that use long-period data, like the broadest-band calculation of source parameters, are prone to error if non-linear behavior at these periods is not identified. Thus it is important to keep in mind the instrument limitations identified in this paper. Future generations of broadband sensors should be thoroughly tested to ensure that any long-period data they record are actually the result of ground motions at those frequencies. To the extent that seismic vaults and/or installation techniques are found to be at fault, these will have to be amended for use at regional distances and moderate earthquakes.

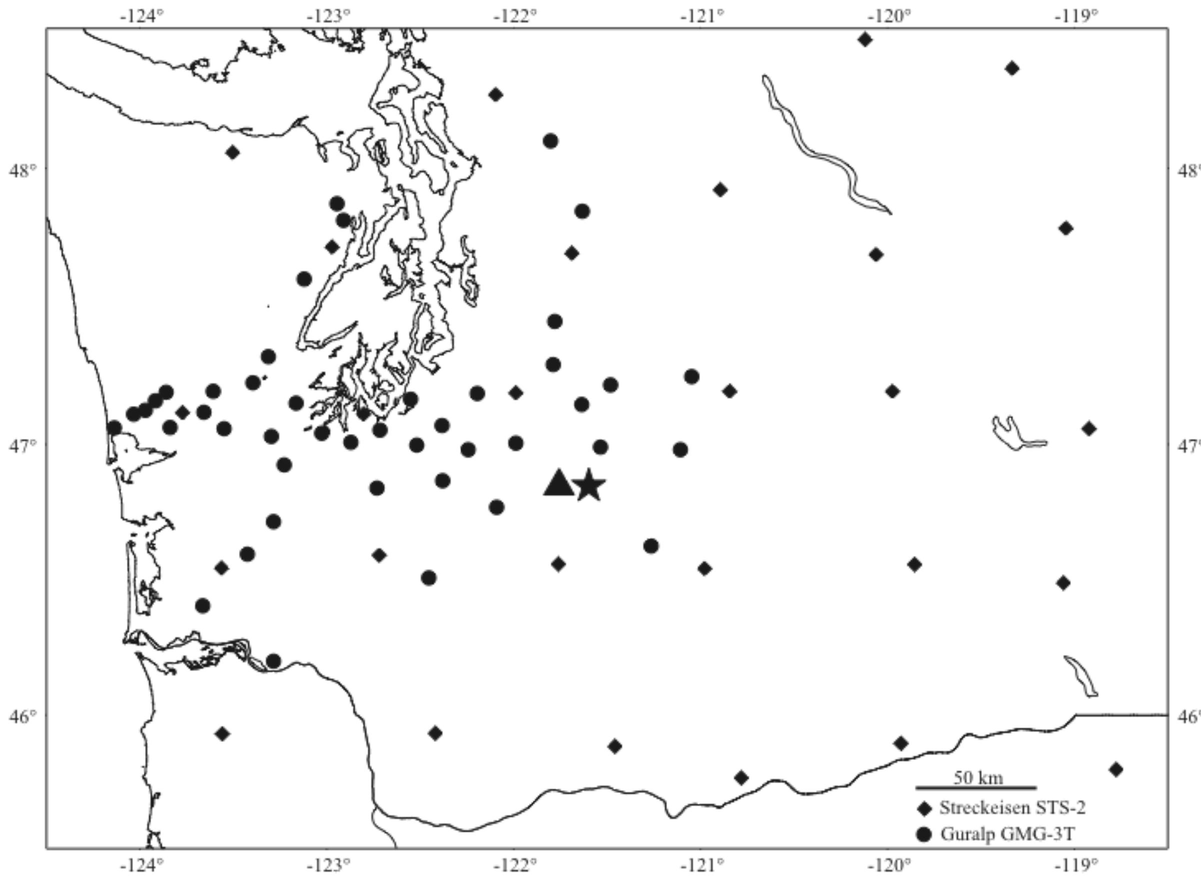

Figure D 1. Rainier Event

Stations of the EarthScope Transportable Array and CAFE experiment.
Diamonds represent the locations of Streckeisen STS-2 instruments and circles represent the locations of Guralp CMG3T instruments. The star represents the location of the Mount Rainier event and the triangle represents the location of Mount Rainier.

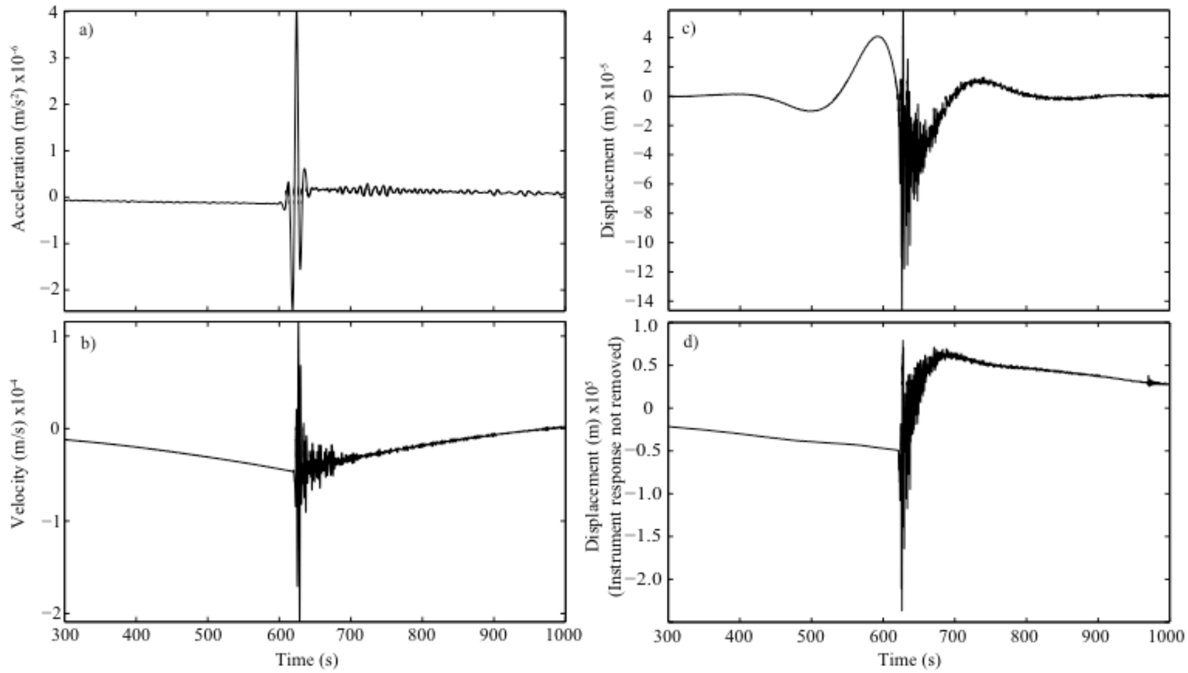

Figure D 2. Station N110, Component BHN

Typical non-linear behavior is identified by a step in the acceleration, (a), followed by a recovery with a period of hundreds of seconds. Non-linear behavior can also be seen in velocity (b), displacement (c) and in raw displacement (integrated velocity response) (d). The data have been low-pass filtered with corner frequencies of 0.1 Hz for acceleration, 0.5 Hz for velocity, and 1 Hz for displacement. The location of station N110 is indicated by a square on figure 3.

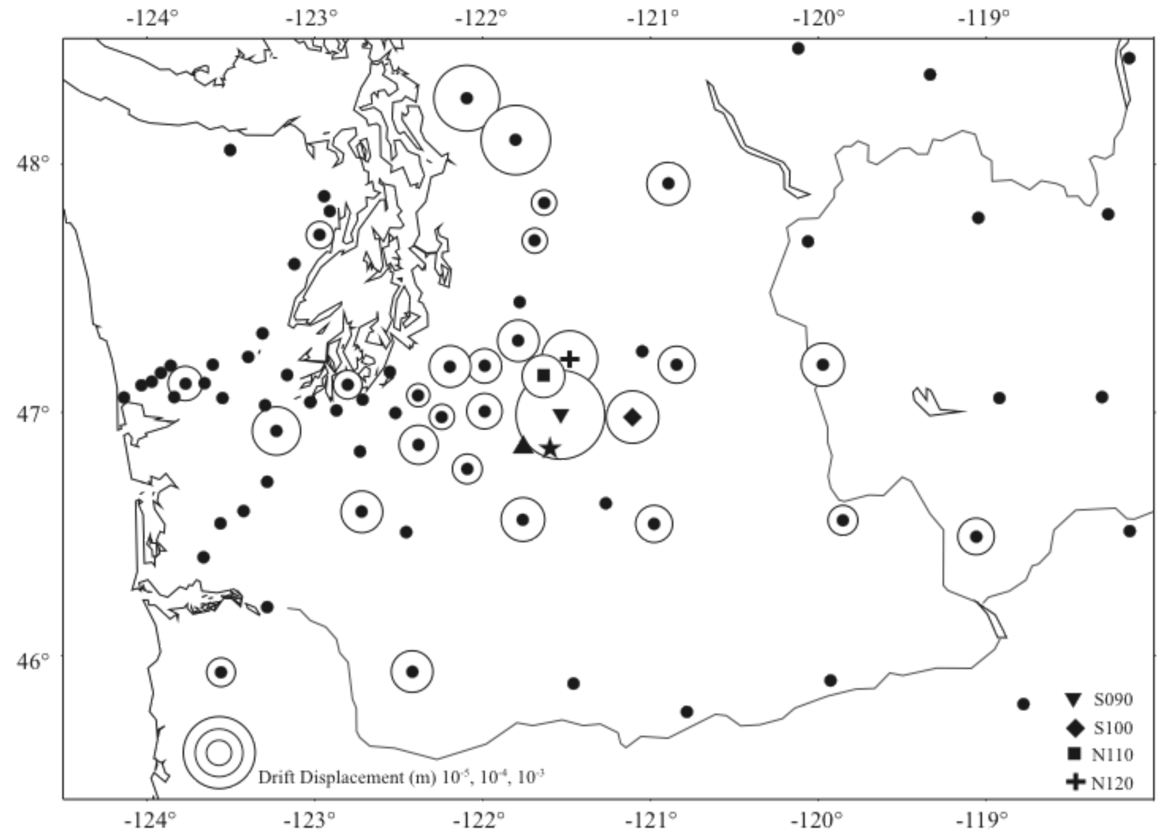

Figure D 3. Rainier Event Drift Amplitudes

CAFE and Earthscope stations near the Mt. Rainier event with drift displacements
Drift displacement is determined by viewing the displacement response and determining how much the mean of the signal drifts from zero. See Figure 2c for an example. The star represents the location of the Mount Rainier event and the triangle represents the location of Mount Rainier. The upside-down triangle represents the location of station S090, the diamond represents the location of station S100, and the square represents the location of station N110. Circle size indicates the relative drift magnitude using a log scale.

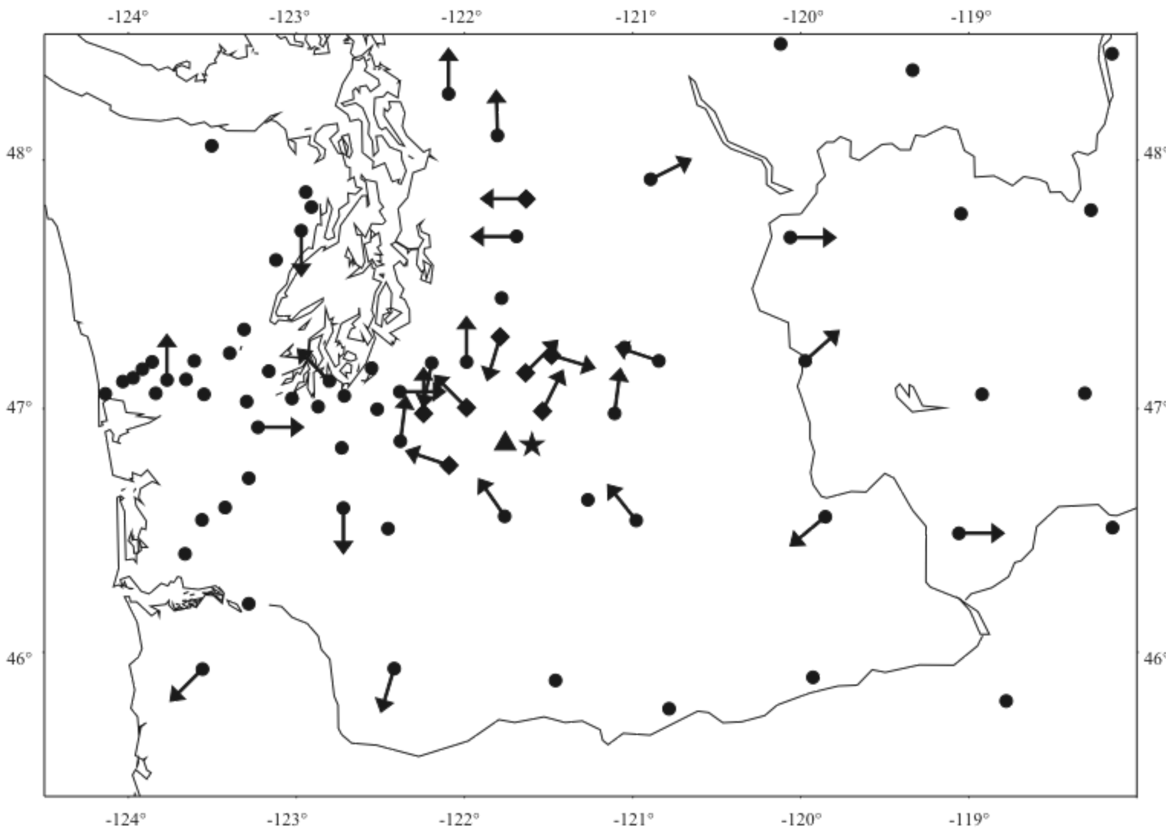

Figure D 4. Rainier Event Drift Polarization

The triangle is the location of Mount Rainier. The star represents the location of the Rainier event. The arrows indicate the polarization direction of the horizontal instrument drifts. The stations plotted as diamonds are stations that had drifts on the vertical component.

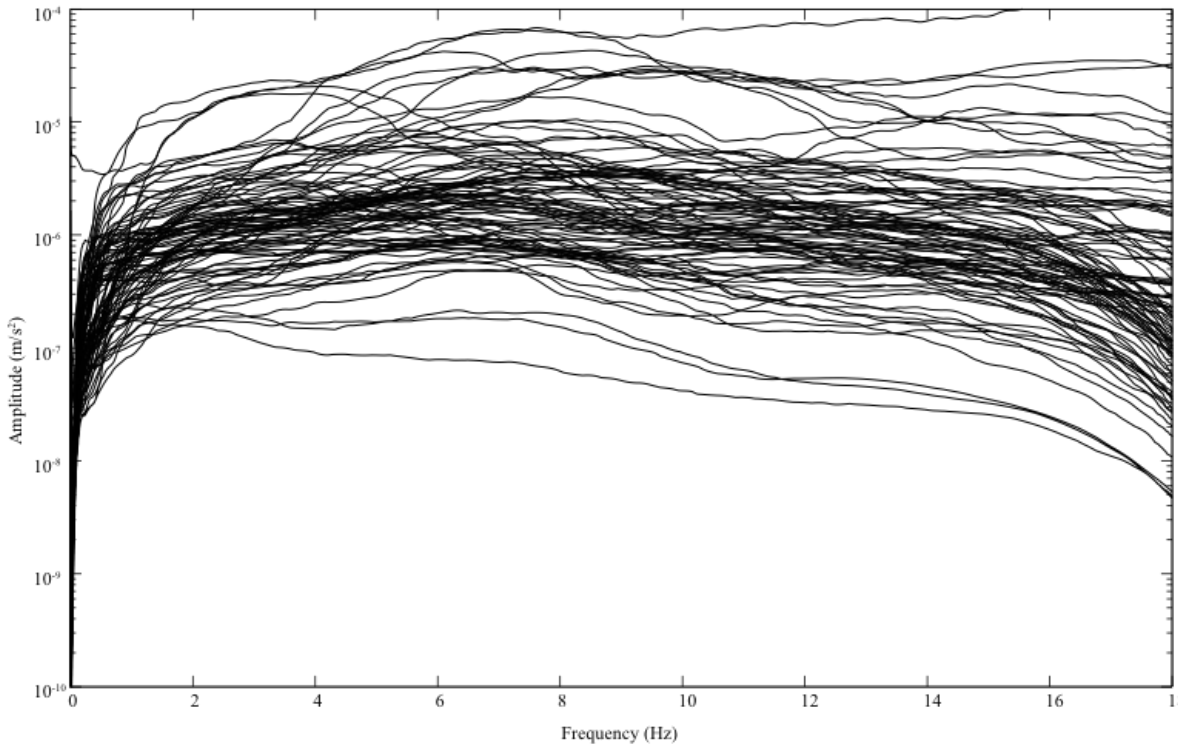

Figure D 5. Non-linear Stations

Acceleration as a function of frequency for stations recording the Rainier event
Only stations that show non-linear behavior are shown.

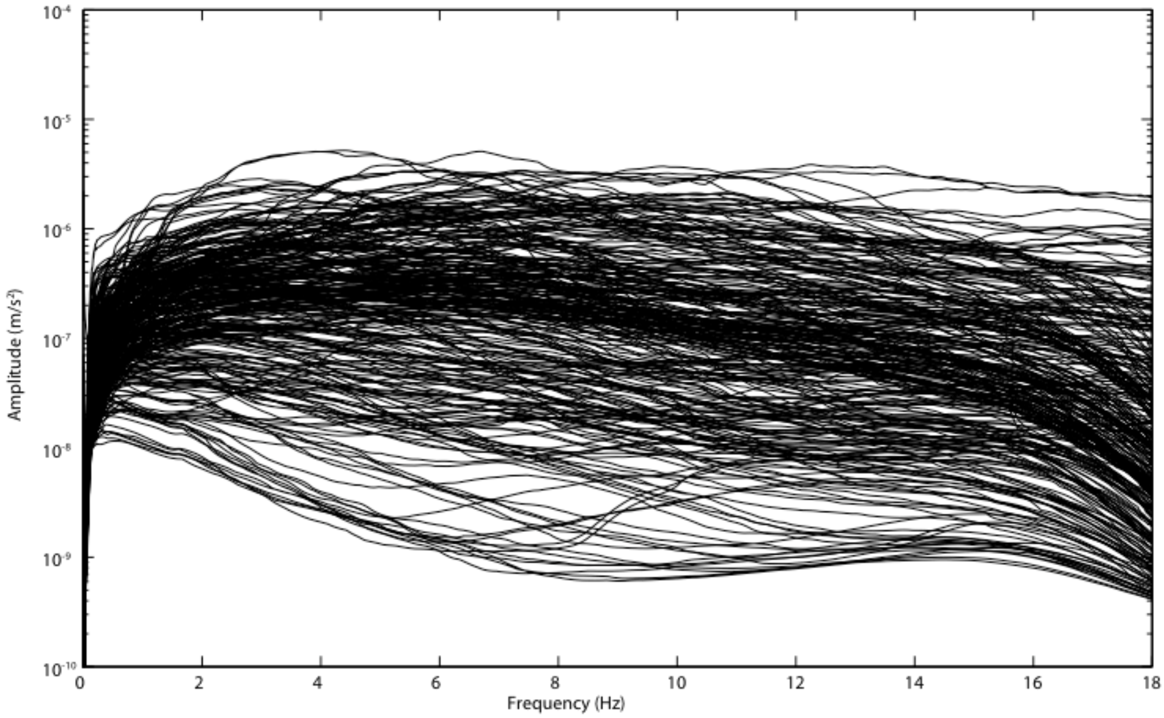

Figure D 6. Linear Stations

Acceleration as a function of frequency for stations recording the Rainier event
Only stations that do not show non-linear behavior are shown.

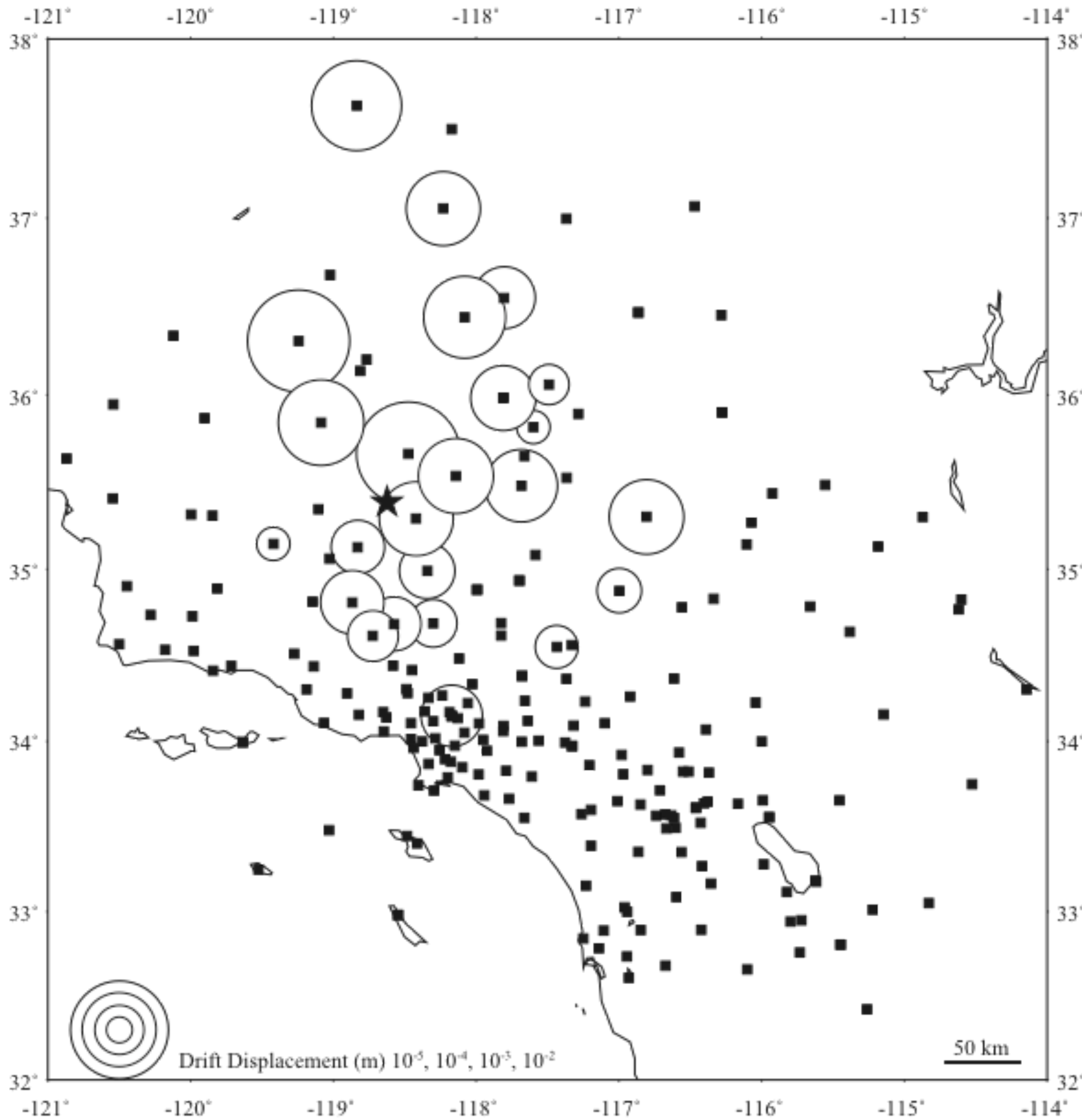

Figure D 7. California Event Drift Amplitudes

Shown are drift displacements for California event (09/29/2004, M5.0). Drift displacement is determined by viewing the displacement response and determining how much the mean of the signal drifts from zero. See Figure 2c for an example. The earthquake location is indicated a star. Circle size indicates the relative drift amplitude using a log scale

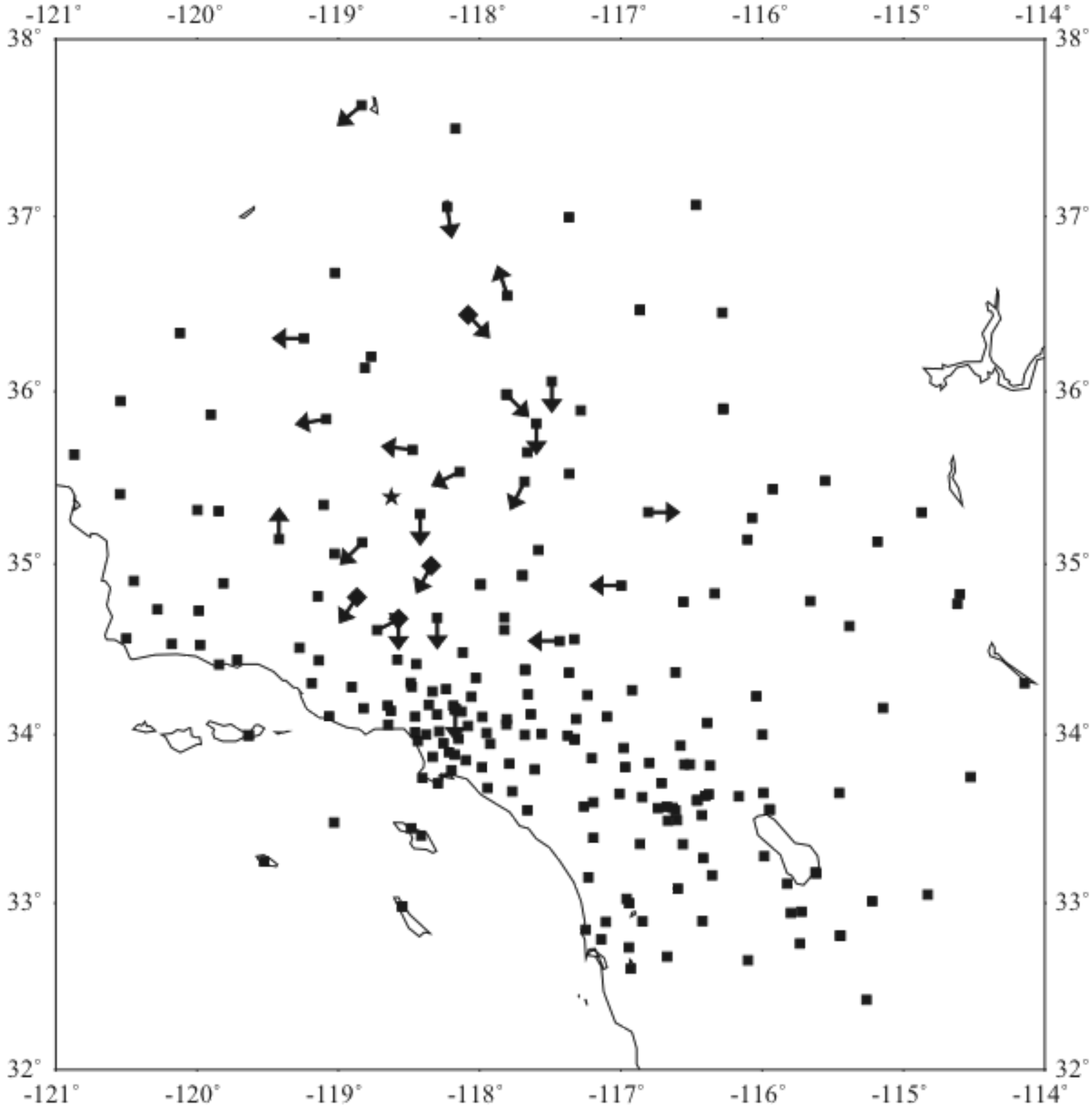

Figure D 8. California Event Drift Polarizations

Shown are the polarization directions of the horizontal instrument drifts for California event (09/29/2004, M5.0). The earthquake location is indicated by a star. The arrows indicate the polarization direction of the horizontal instrument drifts. The stations plotted as diamonds are stations that had drifts on the vertical component.

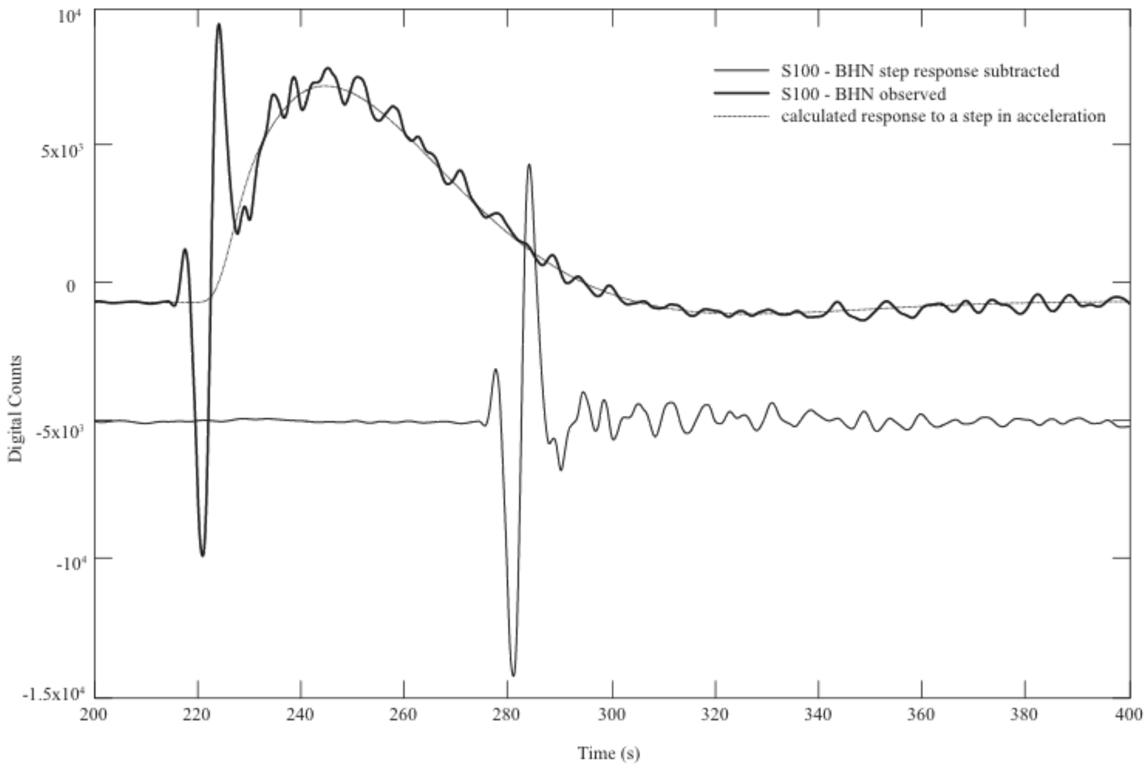

Figure D 9. Tilt Modeling

The signal recorded on station S100 (BHN) is almost an ideal acceleration step response – so much so that an analytic step expression does an excellent job of removing it, resulting in a corrected, interpretable seismogram. The signals are shifted in time for clarity. The location of station S100 is indicated by a diamond on figure D3.

Conclusions

The main focus of this research is to directly observe the shear wave velocity structure of the Seattle Basin for the purposes of assisting in the prediction of ground motions during damaging earthquakes. I used a legacy dataset and was able to image the top 4-5 km of the Seattle Basin with 5-7 km resolution in downtown Seattle with lessor resolution in surrounding areas. Moving forward, I believe that this method is very promising for imaging other urban areas in earthquake country whether or not they sit in basins.

One major challenge for Seattle is that it sits on a particularly deep basin. To image all the way down to the bottom of the Seattle Basin with Rayleigh waves, I would need good coverage down to a period of about 20 seconds. In order to use 20 second Rayleigh waves the station spacing would need to be over 100 km. There must be at least one and preferably two or more wavelengths in between stations to obtain reliable phase velocity measurements. In order to have good coverage over a square model area with 100 km on each side, I would need around 60-80 stations. In addition, if 1-km resolution is desired in the urban area, additional stations would be needed in the interior of the model space. Due to the periods observed, broadband instruments are required. So, this experiment would require close to 100 broadband instruments to meet the requirements of imaging the entire basin with high enough resolution in the urban area to distinguish differences on the scale of urban neighborhoods. If the Seattle Basin were only half as deep as 9 km, the station requirement would be reduced by around 20-30 stations. One important benefit of this station plan is that it would encompass several other basins in the Puget Lowland, including the Tacoma and Everett Basins. Additional stations could be used to improve resolution in these additional urban areas. A possible station configuration, using the same number of stations as the SHIPS array is shown in Figure E1.

Alternatively, if it is not important to image all the way to the bottom of the basin or if a large broadband array is not available, one could use short period instruments in a tighter configuration to observe only the top few kilometers. The main difficulty in this configuration is solving the cycle-skipping problem of surface waves. One would need to have a reasonably good shear wave velocity model at depths just below the layers to be imaged in order to set the Rayleigh wave phase velocity for the longest period in the same way that I did. The cycle-skipping problem does not exist when using longer periods because skipping a cycle will result in unreasonably fast or slow velocities at those periods. By decreasing the period in small increments from a known point, one can determine the proper phase velocity, avoiding the cycle-skipping problem.

Large broadband arrays have been deployed to observe many different scientifically interesting Earth structures. It would be useful to the seismic hazard community to use this power to make observations of sedimentary basins.

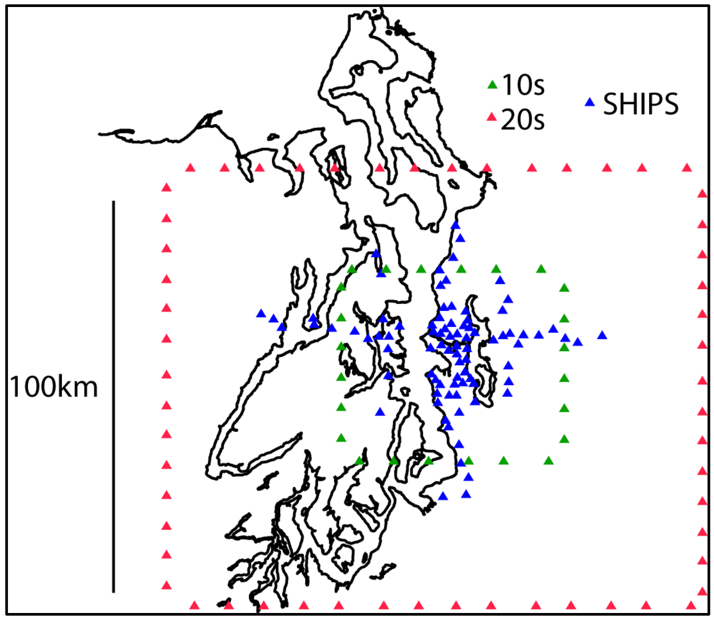

Figure E 1. Suggested Station Configuration

Suggested station configuration for a broadband array to image the Seattle Basin using noise-correlation Rayleigh waves. The red stations indicate spacing required to resolve 20 second Rayleigh waves and the green stations indicate spacing required to resolve 10 second waves. SHIPS array stations are in blue.

Bibliography

Atwater, B. F. (1992), Geologic evidence for earthquakes during the past 2000 years along the Copalis River, southern coastal Washington, *J Geophys Res*, *97*(B2), 1901-1919.

Barberopoulou, A., A. Qamar, T. L. Pratt, K. C. Creager, and W. P. Steele (2004), Local amplification of seismic waves from the Denali earthquake and damaging seiches in Lake Union, Seattle, Washington, *Geophys. Res. Lett.*, *31*(3), 5.

Battaglia, J., K. Aki, and J. P. Montagner (2000), Tilt signals derived from a GEOSCOPE VBB station on the Piton de la Fournaise Volcano, *Geophys. Res. Lett.*, *27*(5), 605-608.

Bensen, G. D., M. H. Ritzwoller, M. P. Barmin, A. L. Levshin, F. Lin, M. P. Moschetti, N. M. Shapiro, and Y. Yang (2007), Processing seismic ambient noise data to obtain reliable broad-band surface wave dispersion measurements, *Geophys J Int*, *169*(3), 1239-1260.

Blakely, R. J., R. E. Wells, C. S. Weaver, and S. Y. Johnson (2002), Location, structure, and seismicity of the Seattle fault zone, Washington; evidence from aeromagnetic anomalies, geologic mapping, and seismic-reflection data, *Bull. Geol. Soc. Am.*, *114*(2), 169-177.

Boore, D. M., C. D. Stephens, and W. B. Joyner (2002), Comments on baseline correction of digital strong-motion data; examples from the 1999 Hector Mine, California, earthquake, *Bull. Seism. Soc. Am.*, *92*(4), 1543-1560.

Booth, D. B. (1994), Glaciofluvial infilling and scour of the Puget Lowland, Washington, during ice-sheet glaciation, *Geology*, *22*(8), 695-698.

Brocher, T. M., et al. (2001), Upper crustal structure in Puget Lowland, Washington; results from the 1998 seismic hazards investigation in Puget Sound, *J Geophys Res*, *106*(B7), 13.

Clinton, J. F., S. C. Bradford, T. H. Heaton, and J. Favela (2006), The Observed Wander of the Natural Frequencies in a Structure, *Bull. Seism. Soc. Am.*, *96*, 237-257.

Delorey, A. A., J. Vidale, J. Steim, and P. Bodin (2008), Broadband sensor nonlinearity during moderate shaking, *Bull. Seism. Soc. Am.*, *98*(3), 1595-1601.

Eberhard, M. O., J. De la Colina, and S. Ryter (1995), Seismic Vulnerability of the Alaskan Way Viaduct: WSDOT Typical Unit, edited, Department of Transportation, Olympia, WA.

Frankel, A. D., D. L. Carver, and R. A. Williams (2002), Nonlinear and linear site response and basin effects in Seattle for the M 6.8 Nisqually, Washington, earthquake, *Bull. Seism. Soc. Am.*, *92*(6), 2090-2109.

Frankel, A. D., W. J. Stephenson, and D. Carver (2009), Sedimentary Basin Effects in Seattle, Washington: Ground-Motion Observations and 3D Simulations, *Bull. Geol. Soc. Am.*, *99*(3), 1579-1611.

Frankel, A. D., D. L. Carver, E. Cranswick, M. E. Meremonte, T. Bice, and D. E. Overturf (1999), Site response for Seattle and source parameters of earthquakes in the Puget Sound region, *Bull. Seism. Soc. Am.*, *89*(2), 468-483.

Frankel, A. D., W. J. Stephenson, D. L. Carver, R. A. Williams, J. K. Odum, and S. Rhea (2007), Seismic hazard maps for Seattle, Washington, incorporating 3D sedimentary basin effects, nonlinear site response, and rupture directivity, *U.S. Geological Survey Open-File Report 2007-1175*.

Frankel, A. D., C. Mueller, T. Barnhard, D. Perkins, E. V. Leyendecker, N. Dickman, S. Hanson, and M. Hopper (1996), National Seismic-Hazard Maps: Documentation June 1996, *Open File Rep U S Geol Surv*, *96-532*.

Goldfinger, C., C. H. Nelson, and J. E. Johnson (2003), Deep-water turbidites as Holocene earthquake proxies: the Cascadia subduction zone and Northern San Andreas Fault systems, *Ann Geophys*, *46*(5), 1169-1194.

Graizer, V. (2006), Tilts in strong ground motion, *Bull. Seism. Soc. Am.*, *96*(6), 2090-2102.

Graves, R., A. Pitarka, and P. G. Somerville (1998), Ground-motion amplification in the Santa Monica area: effects of shallow basin-edge structure, *Bull. Geol. Soc. Am.*, *88*, 1224-1242.

Hartzell, S., D. Carver, E. Cranswick, and A. D. Frankel (2000), Variability of site response in seattle, Washington, *Bull. Seism. Soc. Am.*, *90*(5), 1237-1250.

Haugerud, R. A., D. J. Harding, S. Y. Johnson, J. L. Harless, C. S. Weaver, and B. L. Sherrod (2003), High-resolution lidar topography of the Puget Lowland, Washington, *GSA Today*, *13*(6), 4-10.

Ichinose, G. A., H. K. Thio, and P. G. Somerville (2004), Rupture process and near-source shaking of the 1965 Seattle-Tacoma and 2001 Nisqually, intraslab earthquakes, *Geophys. Res. Lett.*, *31*, L10604.

Johnson, S. Y., C. J. Potter, J. M. Armentrout, J. J. Miller, C. A. Finn, and C. S. Weaver (1996), The southern Whidbey Island Fault; an active structure in the Puget Lowland, Washington, *Bull. Geol. Soc. Am.*, *108*(3), 334-354.

Knaebel, P., M. O. Eberhard, and J. De la Colina (1995), Seismic Vulnerability of the Alaskan Way Viaduct: SED Typical Unit, edited, Department of Transportation, Olympia, WA.

Kramer, S. L., and M. O. Eberhard (1995), Seismic Vulnerability of the Alaskan Way Viaduct - Summary Report, edited, Washington Department of Transportation, Olympia, WA.

Kramer, S. L., N. Sivaneswaran, and K. M. Tucker (1995), Seismic Vulnerability of the Alaskan Way Viaduct: Geotechnical Engineering Aspects, edited, Department of Transportation, Olympia, WA.

Lees, J. M., and R. S. Crosson (1990), Tomographic Imaging of Local Earthquake Delay Times for 3-Dimensional Velocity Variation in Western Washington, *J Geophys Res*, *95*(B4), 4763-4776.

Li, Q., W. S. D. Wilcock, T. L. Pratt, C. M. Snelson, and T. M. Brocher (2006), Seismic attenuation structure of the Seattle basin, Washington State, from explosive-source refraction data, *Bull. Seism. Soc. Am.*, *96*(2), 553-571.

Liu, P. C., and R. J. Archuleta (2002), The effect of a low-velocity surface layer on simulated ground motion, *Seismol Res Lett*, *73*, 267.

Mazzotti, S., H. Dragart, R. D. Hyndman, M. M. Miller, and J. A. Henton (2002), GPS deformation in a region of high crustal seismicity: N Cascadia forearc, *Earth Planet Sci Lett*, *198*(1-2), 41-48.

Michel, C., and P. Gueguen (2010), Time-Frequency Analysis of Small Frequency Variations in Civil Engineering Structures Under Weak and Strong Motions Using a Reassignment Method, *Struct. Health Monit.*, *9*(2), 159-171.

Murray, J., and J. Langbein (2004), Slip on the San Andreas Fault at Parkfield, California, over two earthquake cycles, and the implications for seismic hazard, *Bull. Geol. Soc. Am.*, *96*(4B), 5283-5303.

Nelson, A. R., S. Y. Johnson, H. M. Kelsey, R. E. Wells, B. L. Sherrod, S. K. Pezzopane, L. A. Bradley, R. D. Koehler, and R. C. Bucknam (2003), Late Holocene earthquakes on the Toe Jam Hill fault, Seattle fault zone, Bainbridge Island, Washington, *Geol. Soc. Am. Bull.*, *115*(11), 1388-1403.

Pitarka, A., R. Graves, and P. Somerville (2004), Validation of a 3D Model of the Puget Sound Region Based on Modeling Ground Motion from the 28 February 2001 Nisqually Earthquake, *Bull. Geol. Soc. Am.*, *94*(5), 1670-1689.

Pondard, N., R. Armijo, G. C. P. King, B. Meyer, and F. Flerit (2007), Fault interactions in the Sea of Marmara pull-apart (North Anatolian Fault); earthquake clustering and propagating earthquake sequences, *Geophys J Int*, *171*(3), 1185-1197.

Pratt, T. L., S. Y. Johnson, C. J. Potter, W. J. Stephenson, and C. A. Finn (1997), Seismic reflection images beneath Puget Sound, western Washington State; the Puget Lowland thrust sheet hypothesis, *J Geophys Res*, *102*(B12), 27,469-427,489.

Pratt, T. L., T. M. Brocher, C. S. Weaver, K. C. Creager, C. M. Snelson, R. S. Crosson, K. C. Miller, and A. M. Trehu (2003a), Amplification of seismic waves by the Seattle Basin, Washington State, *Bull. Seism. Soc. Am.*, *93*(2), 533-545.

Pratt, T. L., K. L. Meagher, T. M. Brocher, T. Yelin, R. D. Norris, L. Hultgrien, E. A. Barnett, and C. S. Weaver (2003b), Earthquake recordings from the 2002 Seattle Seismic Hazard Investigation of Puget Sound (SHIPS), Washington State, *Open File Rep U S Geol Surv*, 72.

Riddihough, R. P. (1984), Recent movements of the Juan de Fuca plate system, *J Geophys Res*, *89*(B8), 6980-6994.

Satake, K., K. Wang, and B. F. Atwater (2003), Fault slip and seismic moment of the 1700 Cascadia earthquake inferred from Japanese tsunami descriptions, *J Geophys Res*, *108*(B11), 17.

Schultz, A. P., and R. S. Crosson (1996), Seismic velocity structure across the central Washington Cascade Range from refraction interpretation with earthquake sources, *J Geophys Res*, *101*(B12), 27,899-827,915.

Sherrod, B. L., T. M. Brocher, C. S. Weaver, R. C. Bucknam, R. J. Blakely, H. M. Kelsey, A. R. Nelson, and R. Haugerud (2004), Holocene fault scarps near Tacoma, Washington, USA, *Geology*, *32*(1), 9-12.

Simpson, D. W. (2006), USArray: an observational and integrative foundation for EarthScope, *Eos Trans. AGU*, *87*(52), Abstract #T42A-01.

Snelson, C. M., T. M. Brocher, K. C. Miller, T. L. Pratt, and A. M. Trehu (2007), Seismic Amplification within the Seattle Basin, Washington State: Insights from SHIPS Seismic Tomography Experiments, *Bull. Seism. Soc. Am.*, *97*(5), 1432-1448.

Stephenson, W. J. (2007), Velocity and density models incorporating the Cascadia Subduction Zone for 3D earthquake ground motion simulation, *Open File Rep U S Geol Surv*, *2007-1348*.

Stephenson, W. J., A. Frankel, J. K. Odum, R. A. Williams, and T. L. Pratt (2006), Towards resolving an earthquake ground motion mystery in west Seattle, Washington state:

shallow seismic focusing may cause anomalous chimney damage, *Geophys. Res. Lett.*, *33*(6), L06316.

Symons, N. P., and R. S. Crosson (1997), Seismic velocity structure of the Puget Sound region from 3-D non-linear tomography, *Geophys. Res. Lett.*, *24*(21), 2593-2596.

Takeuchi, H., and M. Saito (1972), Seismic Surface Waves, in *Methods in Computational Physics*, edited, pp. 217-195.

ten Brink, U. S., J. Song, and R. C. Bucknam (2006), Rupture models for the A.D. 900-930 Seattle Fault earthquake from uplifted shorelines, *Geology*, *34*(7), 585-588.

ten Brink, U. S., P. C. Molzer, M. A. Fisher, R. J. Blakely, R. C. Bucknam, T. Parsons, R. S. Crosson, and K. C. Creager (2002), Subsurface geometry and evolution of the Seattle fault zone and the Seattle Basin, Washington, *Bull. Seism. Soc. Am.*, *92*(5), 1737-1753.

Wells, R. E., and R. W. Simpson (2001), Northward migration of the Cascadia forearc in the northwestern U. S. and implications for subduction deformation, *Earth Planets Space*, *53*(4), 275-283.

Wells, R. E., C. S. Weaver, and R. J. Blakely (1998), Fore-arc migration in Cascadia and its neotectonic significance, *Geology*, *26*(8), 759-762.

Wielandt, E., and T. Forbriger (1999), Near-field seismic displacement and tilt associated with the explosive activity of Stromboli, *Annali di Geofisica*, *42*(3), 407-416.

Wiens, D. A., S. H. Pozgay, P. J. Shore, A. W. Sauter, and R. A. White (2005), Tilt recorded by a portable broadband seismograph; the 2003 eruption of Anatahan Volcano, Mariana Islands, *Geophys. Res. Lett.*, *32*(18).

Witter, R. C., H. M. Kelsey, and E. Hemphill-Haley (2003), Great Cascadia earthquakes and tsunamis of the past 6700 years, Coquille River estuary, southern coastal Oregon, *Bull. Geol. Soc. Am.*, *115*(10), 1289-1306.

Zahradnik, J., and A. Plesinger (2005), Long-period pulses in broadband records of near earthquakes, *Bull. Seism. Soc. Am.*, *95*(5), 1928-1939.

VITA

Andrew Delorey was born in Melrose, Massachusetts. He lived all of his childhood in Wakefield, Massachusetts, and then earned a Bachelor of Science in Mechanical Engineering from Tufts University in Medford, Massachusetts in 1992. He worked in the software industry in California for ten years before leaving this career to travel the world for a year. Upon returning to the United States, he earning a Master of Science in Geology and Geophysics from the University of Hawaii in 2003. In 2010 he earned a Doctor of Philosophy at the University of Washington in Earth and Space Sciences, specializing in seismology.